REVIEW

Single particle electron cryomicroscopy: trends, issues and future perspective

Kutti R. Vinothkumar and Richard Henderson*

MRC Laboratory of Molecular Biology, Francis Crick Avenue, Cambridge CB2 0QH, UK

Abstract. There has been enormous progress during the last few years in the determination of three-dimensional biological structures by single particle electron cryomicroscopy (cryoEM), allowing maps to be obtained with higher resolution and from fewer images than required previously. This is due principally to the introduction of a new type of direct electron detector that has 2- to 3-fold higher detective quantum efficiency than available previously, and to the improvement of the computational algorithms for image processing. In spite of the great strides that have been made, quantitative analysis shows that there are still significant gains to be made provided that the problems associated with image degradation can be solved, possibly by minimising beam-induced specimen movement and charge build up during imaging. If this can be achieved, it should be possible to obtain near atomic resolution structures of smaller single particles, using fewer images and resolving more conformational states than at present, thus realising the full potential of the method. The recent popularity of cryoEM for molecular structure determination also highlights the need for lower cost microscopes, so we encourage development of an inexpensive, 100 keV electron cryo-microscope with a high-brightness field emission gun to make the method accessible to individual groups or institutions that cannot afford the investment and running costs of a state-of-the-art 300 keV installation. A key requisite for successful high-resolution structure determination by cryoEM includes interpretation of images and optimising the biochemistry and grid preparation to obtain nicely distributed macromolecules of interest. We thus include in this review a gallery of cryoEM micrographs that shows illustrative examples of single particle images of large and small macromolecular complexes.

* Author for correspondence: Richard Henderson, MRC Laboratory of Molecular Biology, Francis Crick Avenue, Cambridge CB2 0QH, UK. Email: rh15@mrc-lmb.cam.ac.uk

1. Introduction

Electron cryomicroscopy (cryoEM) of biological structures has grown to become a powerful technique for three-dimensional (3D) structure determination of biological molecules. Figures 1–3 show three recent examples of single particle cryoEM structure determinations that span the range from large highly symmetrical viruses to ribonucleoprotein complexes and membrane proteins. In this review, we discuss progress over the last few years and identify some of the key issues that may be important in producing further improvements over the next few years. In addition to the topics we highlight here, there are other technical developments that have the potential to improve cryoEM. These include the development of phase plates (Danev *et al.* 2014; Glaeser, 2013; Murata *et al.* 2010; Nagayama, 2014), Cc correctors (Kabius *et al.* 2009) and cooling to liquid helium temperature (Fujiyoshi, 1998) provided that the problems of beam-induced movement can be minimised. There are also valuable publications that focus on specific issues, including map validation (Rosenthal & Rubinstein, 2015), specimen preparation (Glaeser *et al.* 2016; Glaeser, 2016), electron cryotomography (Gan & Jensen, 2012; Medalia *et al.* 2002) and finally three volumes of Methods in Enzymology covering a wide range of topics in more detail (Volumes 481, 482, 483, published in 2010).

2. Historical overview

CryoEM has drawn strength gradually from a series of contributing ideas and observations, from both academia and industry. These are briefly summarised below.

2.1 The path to CryoEM

Electrons and electron microscopy (EM) have the power to image individual atoms. In the study of inorganic materials, resolutions better than 1 Ångstrom are routinely achieved. However, this requires high-electron doses and Glaeser (1971) pointed out that radiation damage by the electron beam meant that structure determination of organic and biological molecules, such as valine and adenine, would require averaging multiple molecular images and suggested that this could be done by recording images from crystals and averaging over many unit cells. Unwin & Henderson determined the 3D structure of bacteriorhodopsin to 7 Å resolution by averaging data from images of unstained 2D crystals of bacteriorhodopsin (purple membrane) at room temperature (Unwin & Henderson, 1975; Henderson & Unwin, 1975). Taylor & Glaeser (1974) showed that diffraction patterns and images (Taylor & Glaeser, 1976) of frozen catalase crystals cooled to −120 °C could be recorded with longer exposures than at higher temperatures and would thus give more information due to the reduced effect of radiation damage. In the 1970s, the X-ray crystallographic community also adopted crystal cooling to preserve diffraction from crystals for longer both for small organic molecules and for protein and nucleic acid crystals (Haas & Rossmann, 1970; Thomanek *et al.* 1973; Petsko, 1975).

The biggest step forward came from the extensive work by Dubochet and his colleagues at European Molecular Biology Laboratory (EMBL) in the early 1980s when they investigated in the electron microscope the properties of thin films of water rapidly frozen at different freezing rates and different temperatures. They characterised vitreous, cubic and hexagonal forms of ice, and developed a simple plunge-freezing method for preparing grids (Adrian *et al.* 1984; Dubochet *et al.* 1982, 1984). Their work depended on the development of the first ultra-high vacuum specimen environment in the Philips 400 electron microscope, which had been required by the materials science community to avoid contamination of their clean metallic specimens. Dubochet *et al.* (1988) showed that beautiful images of a whole series of structures from ferritin to adenovirus could be recorded after rapidly freezing EM grids on which thin suspensions of the structures in normal aqueous buffer had been made by application of a small drop followed by blotting and plunge-freezing into liquid ethane. They also

2
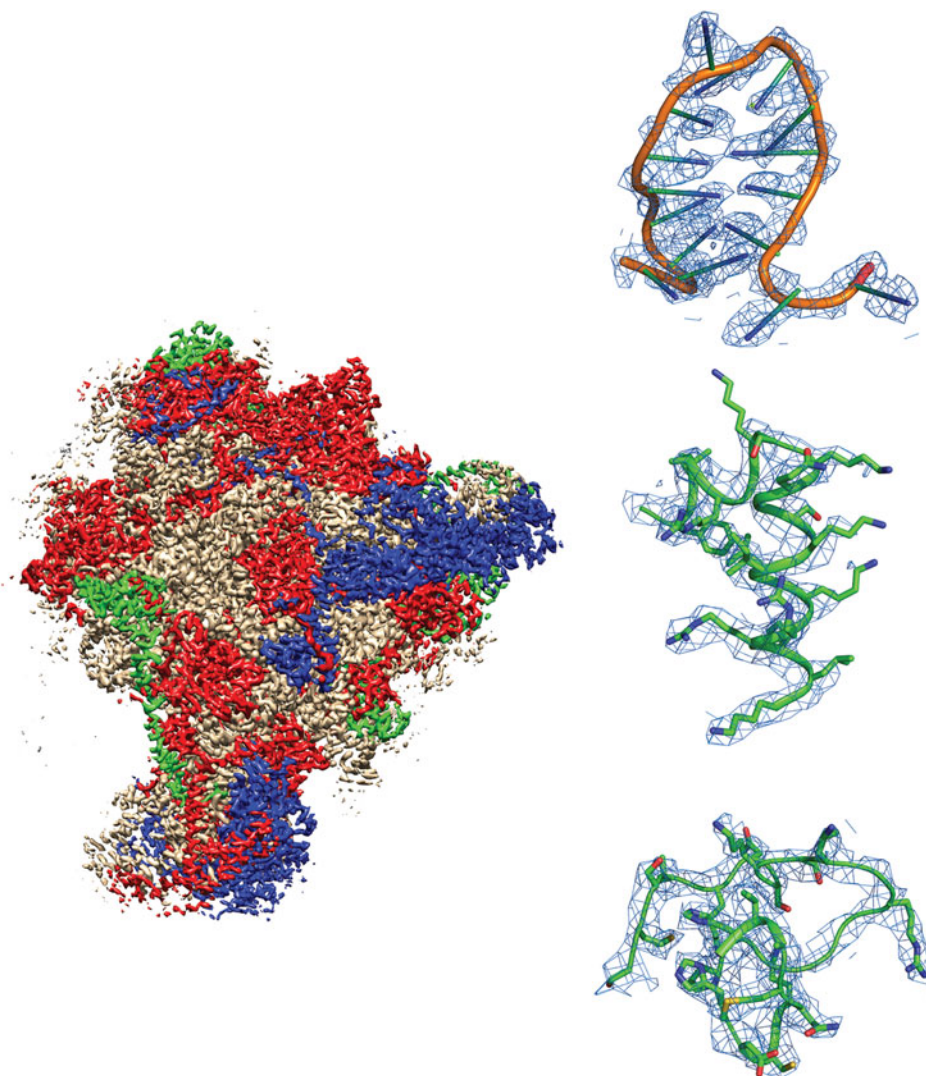
Fig. 1. Example of a recently-published single-particle cryoEM structure, with images collected using FEI Falcon direct electron detector – Mitochondrial ribosome, EMDB-2566 (Amunts *et al.* 2015). Densities are shown for RNA, an α-helix and a loop.

developed an efficient double-blade cold shield that they used to protect the grid once it was in the electron microscope and reduce the rate of surface ice contamination from residual water in the microscope chamber.

Freezing and the use of cryoprotection took longer to become widely adopted for X-ray crystallography. It was not until crystals were cooled to near liquid nitrogen temperature that the full benefit of reduced radiation damage was obtained (Henderson, 1990; Hope & Nichols, 1981; Hope *et al.* 1989).

2.2 Theoretical background

With some simplifying assumptions, Henderson (1995) attempted to calculate from first principles the size of the smallest particle that would allow its orientation to be determined from single particle cryoEM images, if perfect images could be obtained that were limited only by the observed radiation damage rates for organic and biological structures in the electron beam. This showed that it should be possible to determine the orientations of single particles as small as 40 kDa and to determine the structure at 3 Å resolution using images of about 12 000 single particles, and less images if the particles had internal symmetry. This calculation was done with the criterion that the structure factors (amplitudes and phases of the Fourier components of the structure) should be recorded with a signal-to-noise ratio of 3. Later Rosenthal & Henderson (2003) argued that, since the X-ray protein crystallography community had agreed upon a figure-of-merit of 0.5 as a threshold criterion of structure factor quality, equivalent to a phase error of 60°, the EM community should adopt the same criterion, which

3
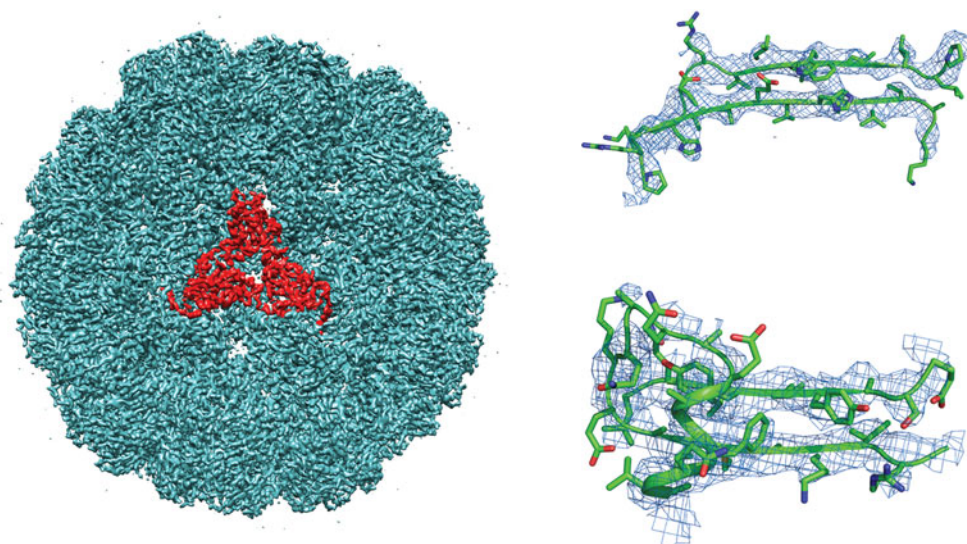
Fig. 2. Example of a recently-published single-particle cryoEM structure, with images collected using Direct Electron DE-12 direct electron detector – Brome mosaic virus, EMDB-6000 (Wang *et al.* 2014). Densities are shown for a α-helix and two β-strands.
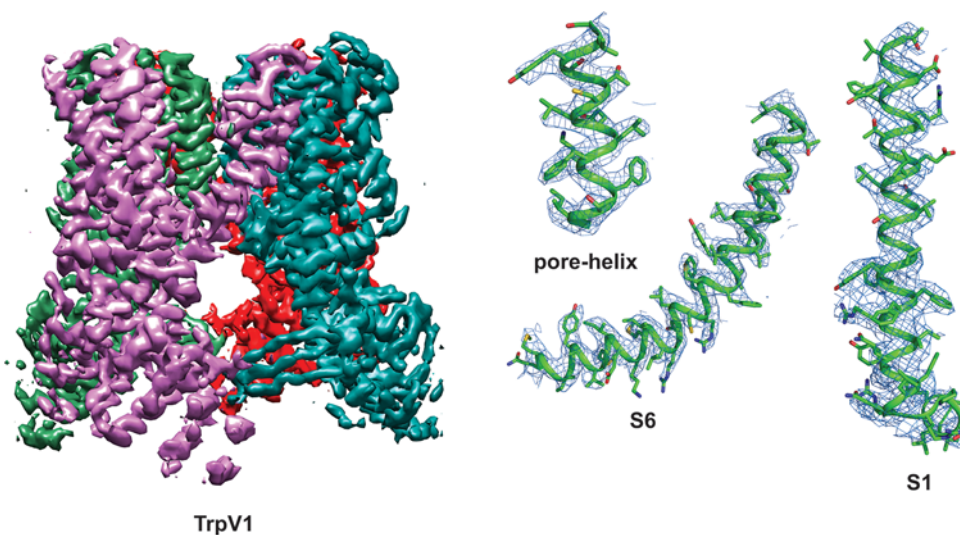
Fig. 3. Example of a recently-published single-particle cryoEM structure, with images collected using Gatan K2 Summit direct electron detector – TRPV1 channels, EMDB-5778 (Liao *et al.* 2013). Densities are shown for three α-helices.

translated into a signal-to-noise ratio of 0.6. This 5-fold reduction in the target signal-to-noise ratio reduced the estimate of the number of required single particle images by a factor of 25 to only 600. They also produced a chart that related the number of particles to the achievable resolution, which depended also on the B-factor that could be used to characterise the resolution-dependent fading of the observed Fourier component amplitudes in real images compared with that expected from theory or electron diffraction. In the interim, Glaeser (1999) also argued that the 3 sigma criterion was too stringent and estimated ∼1400 particles would be required. Of course, these calculations were all approximate and involved a number of simplifying assumptions, but nevertheless they provided a theoretical framework to justify continued efforts to improve the methods being used in practice. Note that the number of particles required is independent of the particle size or molecular weight. For large particles, each single particle image has more contrast than for small particles so fewer images are required to determine the projection structure to a desired accuracy. On the other hand, large particles require more views to sample reciprocal space adequately in three dimensions, according to the πD/d formula of Crowther *et al.* (1970), and these two effects cancel out precisely.

4

2.3 2D-crystalline, helical and single particles with icosahedral symmetry

The poor quality of the electron images of radiation-sensitive organic or biological structures had been noted and quantitative estimates made of the signal loss in images of 2D crystals of paraffin (Henderson & Glaeser, 1985), but good progress with electron crystallography was still possible by averaging the images of many more molecules than suggested by theory. A 3D structure of bacteriorhodopsin at 3.5 Å was obtained by averaging images containing 5 million molecules recorded using film as the detector (Henderson *et al.* 1990). Similar numbers were needed to determine the structure for 2D crystals of light-harvesting complex (LHC) II (Kuhlbrandt *et al.* 1994) and $\alpha\beta$-tubulin zinc sheets (Nogales *et al.* 1998). More recently, following the development of more powerful computer programs that could deal with images of single particles embedded in ice (Spider, Imagic, Electron Micrograph ANalysis (EMAN), Frealign, Xmipp), and faster computational resources that could be parallelised, structures of icosahedral viruses (Grigorieff & Harrison, 2011) and helically-ordered proteins at resolutions beyond 4 Å (Egelman, 2007) were achieved. However, these still required the averaging of images of millions of asymmetric units, in the same way as had been required for 2D crystals. For example, the structure of aquareovirus (Zhang *et al.* 2010) at 3.3 Å that allowed side chains of phenylalanine, tyrosine and tryptophan to be resolved required 80 000 icosahedral viruses, which for a $T = 13$ virus represented 60 million asymmetric units. Rotavirus ($T = 13$) at 3.8 Å also required 10 million asymmetric units (Zhang *et al.* 2008).

The structure of helically ordered protein assemblies in bacterial flagella at 4 Å resolution (Yonekura *et al.* 2003) and of the acetylcholine receptor at a similar resolution (Miyazawa *et al.* 2003) were the two earliest helical structures with relatively high resolution maps. CryoEM of helically ordered assemblies is an active research area with many recent structures reported with resolutions close to 3 Å (Egelman, 2015).

2.4 Single particles without symmetry

Early efforts to use EM for structure determination by combining images of single particles recorded at different specimen tilts came from the group of Hoppe. This involved 3D tomographic imaging of specimens that were relatively stable, including carbon films and heavy-metal-stained molecular assemblies such as fatty acid synthetase (Hoppe *et al.* 1976) or ribosomal subunits (Knauer *et al.* 1983). Frank continued this tradition and with van Heel introduced multivariate statistical methods that allowed 2D averaging and classification, with an accompanying improvement in signal-to-noise ratio of the averaged 2D images (Frank & van Heel, 1982; van Heel & Frank, 1981). The transition from 2D into 3D for single particles without symmetry came with the introduction of angular reconstitution by van Heel (1987) and the Random Conical Tilt (RCT) method by Radermacher *et al.* (1987), allowing 3D structures to be obtained from non-symmetrical particles. The first cryoEM images of ribosomes in projection came in 1988 (Wagenknecht *et al.* 1988b) and in 3D in 1991 (Frank *et al.* 1991). Since then, but prior to the introduction of direct electron detectors, many groups in the ribosome community, in an effort to reach higher resolution on specimens with no internal symmetry, started to collect data sets consisting of several million single particle images (Armache *et al.* 2010; Fischer *et al.* 2010), but found that resolution was limited by specimen and image quality.

2.5 Electronic detectors based on phosphor/fibre-optic/charge-coupled device (CCD)

The introduction of electronic detectors in the 1990s as a replacement for film (Krivanek & Mooney, 1993) for recording images or electron diffraction patterns (Downing & Hendrickson, 1999; Faruqi *et al.* 1999) had both advantages and disadvantages. The advantage was that the microscopist could immediately see the quality of their specimen and thus avoid the long delay between exposure and observing the image that occurred when using film. Film had to be exposed, removed from the microscope, developed, washed, dried, and digitised using a film scanner, though many microscopists became adept at making judgements from images on wet film. The disadvantage was that the first electronic cameras for EM were based on phosphor/fibre-optic/CCD technology, in which the detective quantum efficiency (DQE) was similar to film when used with 80 or 100 keV electrons. At higher voltages, where the microscope resolution, depth-of-focus, aberrations, and beam penetration improve and the undesirable effects of beam-induced specimen charging are less, the DQE of these detectors was actually a lot worse than film. This was especially clear once it became possible to measure the frequency dependence of the DQE (De Ruijter, 1995; Meyer & Kirkland, 2000). Typically the DQE of a phosphor/fibre-optic/CCD electron camera operated at 300 keV was 7–10% at half Nyquist resolution, much lower than film, which has a DQE at half Nyquist of 30–35% when using a 7 μm pixel size (McMullan *et al.* 2009a). As a result, the highest resolution single-particle structures determined prior to 2012 were largely obtained with images recorded on film (Grigorieff & Harrison, 2011; Zhang *et al.* 2010).

2.6 Computer-based image processing

The computational methods used in single particle cryoEM were initially *ad hoc* procedures based on the point group symmetry of the particles being studied. The first cryoEM 3D structure of an icosahedral virus (Vogel *et al.* 1986) at 45 Å resolution used special programs written by Provencher & Vogel (1988). The first cryoEM analysis of clathrin cage structures

5

with D6 symmetry (Vigers *et al.* 1986) at 45 Å resolution used *R*-weighted back-projection from a limited number of cryoEM projections plus 6-fold averaging. Although not strictly single particle cryoEM, Lepault & Leonard (1985) published, including correction for the contrast transfer function (CTF), a 3D structure using cryoEM of individual T4 phage tails, which are single helical particles. A more general approach to computation in 3D EM from images of single particles was started by Frank with the SPIDER package (Frank *et al.* 1981) and van Heel with the Imagic package (van Heel, 1979; van Heel & Keegstra, 1981). Both were widely used on images of negatively stained specimens during the 1980s, especially as mentioned in Section 2.4, after the introduction of angular reconstitution (van Heel, 1987) and RCT (Radermacher *et al.* 1987). The first 3D ribosome structure using cryoEM at 40 Å resolution came in 1991 (Frank *et al.* 1991). EMAN (Ludtke *et al.* 1999; Tang *et al.* 2007) and Frealign (Grigorieff, 1998, 2007) were developed later with explicit treatment of the CTF that would be required to reach high resolution. The first sub-nanometre single particle cryoEM map was obtained by Bottcher *et al.* (1997) at 7.4 Å resolution and by Conway *et al.* (1997) for the hepatitis B virus core, and these structures were calculated with icosahedral-specific programs. The cryoEM structure of the *E.coli* 70S ribosome reached 11.5 Å resolution in the year 2000 (Gabashvili *et al.* 2000). The introduction of maximum likelihood (ML) methods into EM came with papers showing applications in 2D from Sigworth (1998), Scheres *et al.* (2005) and Zeng *et al.* (2007). This was adopted by Scheres (2012) in RELION and most recently by Grigorieff in Frealign (Lyumkis *et al.* 2013). There are now many good packages for single particle cryoEM, which include SPARX (Hohn *et al.* 2007), Simple and Prime (Elmlund & Elmlund, 2012; Elmlund *et al.* 2013), BSOFT (Heymann, 2001) and Xmipp (Marabini *et al.* 1996) as well as those mentioned earlier.

2.7 Field emission guns, column stability and automation

It is illuminating to compare the determination of the structure of adenovirus using cryoEM in 1986 with progress made by 2010. Adrian *et al.* (1984) published the first cryoEM images of adenovirus single particles. Vogel *et al.* (1986) used these images to calculate a map of the structure at 45 Å resolution and Stewart *et al.* (1991) improved this to 35 Å. That early work used cryoEM at 100 keV with a tungsten source and home-made cryo-blades to reduce ice contamination. Twenty-five years later, Liu *et al.* (2010) successfully determined the structure of adenovirus at 3.6 Å resolution. What were the main factors underlying this remarkable improvement? Note that a 10-fold increase in resolution corresponds to a thousand times more information in 3D. Both the earlier and later work used photographic film, so the same medium was used for image recording. In the intervening period, companies such as Philips (subsequently FEI), Hitachi and JEOL had put an enormous amount of development effort into microscope hardware. The key improvements were (a) the introduction of field emission guns (FEGs), which provided a 500-fold increase in brightness that translates into spatial coherence and substantial increase in information transfer at high resolution, (b) the improvement in both column and cold stage stability reducing image drift, (c) the reduction in ice contamination through better vacuum and cryo-shielding, and (d) the increased accelerating voltage from 100 to 300 keV, which reduced the effect of specimen charging, improved the electron-optical performance and gave better depth of focus for thicker specimens like adenovirus. A useful discussion of these factors can be found in Dejong & Vandyck (1993).

Alongside these hardware improvements, the group at Scripps pursued a major development in automated molecular microscopy with the Leginon system (Carragher *et al.* 2000; Suloway *et al.* 2005). This enabled thousands of images to be recorded with the microscope under computer control, using grids with a regular array of holes that had been developed by either Quantifoil (Ermantraut *et al.* 1997, 1998) or Protochips (Stagg *et al.* 2006). This degree of automation helped to produce larger datasets with more particles, and the resulting increase in data compensated for many other sources of information loss. Most recently, FEI have introduced a commercial package for automated cryoEM called EPU, which is helping to produce larger datasets with less human effort. This greater automation was not available for the adenovirus work by Liu *et al.* (2010). Those authors simply used more images, collected manually. Whereas the earlier 1991 structure used only 35 adenovirus particles, the later high-resolution structure in 2010 used 45 000 particles from 1350 micrographs. This extraordinary effort shows just how important automation has now become. The same structure determination could now be carried out more quickly and with much less human effort due to automation.

Finally, it is worth mentioning that one product in particular has come to dominate the recent surge in high-resolution structure determinations. That is the FEI Titan Krios, whose platform itself and the associated developments of optics, stage, vacuum system, and autoloader represent an investment of more than $100 M.

3. Recent advances

3.1 Direct electron CMOS detectors

A big step forward came around 2012–2013 with the introduction of direct electron detectors fabricated using complementary metal oxide semiconductor (CMOS) technology that had been developed over the preceding decade (Faruqi *et al.* 2005;

6

Milazzo *et al.* 2005). These detectors have a rolling-shutter readout mechanism and can read out images continuously with a frame rate that can range from 1 to 1000 Hz or more. The frame rate simply depends on how many parallel analog-to-digital converter (ADC) are used to digitise the voltage on the diode in each pixel, whose voltage is discharged by electron-hole pairs that are created as the incident high energy electron passes through the detector. The effect of radiation damage on the detector can be minimised both by using special radiation-hard design features, but also by increasing the frame rate, since radiation damage increases the leakage current and this is less important at fast frame rates. In addition, these CMOS detectors can be made to be very thin (by backthinning after wafer fabrication), and this reduces the amount of energy deposited in the incorrect pixel of the detector by electrons backscattered from the substrate material, which also adds noise to the image. The modulation transfer function and DQE of a direct electron detector can be improved by a factor of two or more by backthinning (McMullan *et al.* 2009c). The reduction of backscattering also results in a 2- to 3-fold improvement in detector lifetime due to reduced overall energy deposition.

The improved DQE, together with the ability to record high frame-rate movies has brought synergistic advantages. The improved DQE alone provides a significant advantage. The availability of movie recording allows the effect of beam-induced specimen movement and image blurring to be reduced by subsequent alignment and appropriate weighting of the individual frames thus increasing the signal-to-noise ratio of the particle images (Bai *et al.* 2013; Brilot *et al.* 2012; Campbell *et al.* 2012; Grant & Grigorieff, 2015; Li *et al.* 2013a; Rubinstein & Brubaker, 2015; Scheres, 2014; Vinothkumar *et al.* 2014a). These improved motion-corrected images then allow the more accurate determination of the position and orientation of each particle, which produces a 3D map of the structure at higher resolution than it would be without the corrections applied. This higher resolution map then provides a better target for the orientation determination in an iterative manner. Thus the new generation of detectors has arguably produced a bigger impact on the attainable resolution than might have been expected from the increased DQE alone.

3.2 Electron counting

A further improvement in DQE is possible by processing individual frames recorded at very low dose so that single electron events can be identified and their signal replaced either by a delta function at the centroid of the event density at sub-pixel resolution or by applying a more sophisticated procedure (Turchetta, 1993), before summing the frames to produce a normal image or movie (McMullan *et al.* 2009b). Currently the improvement in DQE due to electron counting is most apparent at low resolution (McMullan *et al.* 2014) and can be exploited by recording images at higher magnification than might normally be chosen and carrying out subsequent 2×2 or 3×3 binning. At the time of writing this review, only the Gatan K2 camera has a frame rate that is high enough for robust practical recording of images in counting mode (Li *et al.* 2013a, b), though in principle electron counting can be done using any detector with a high enough signal-to-noise ratio.

3.3 Improved computer programs

Many of the early computer programs for image processing required significant experience for successful operation, and compensation for the effects of the CTF were either ignored or involved special procedures with a limited range of applications. EMAN (Ludtke *et al.* 1999; Tang *et al.* 2007) and Frealign (Grigorieff, 1998, 2007) were the first single particle computational approaches that explicitly included CTF correction at the heart of their operation, which is absolutely required to reach high resolution. The full range of point group symmetries was also embedded in both programs, a feature that had also been available in Imagic since the mid-1980s (van Heel *et al.* 1996).

RELION was developed by Scheres in 2010 and from the start included a very simple graphical user interface (GUI) that allowed the naïve user to make rapid progress without extensive experience (Scheres, 2012). EMAN had a similar GUI from the beginning, which makes these two systems very popular. RELION also included two significant innovations. A regularised ML scoring system, rather than a simple cross-correlation maximisation algorithm, was used to determine the orientations of the individual single particle images, and to calculate the 3D structures. The ML-scoring itself was not new in RELION. It was also present in Xmipp. However, RELION also used regularisation, which leads to optimal weights on the reconstruction and on the alignments. Parameters for these weights are estimated through the empirical Bayesian approach from the data themselves, rather than through tuning by a user. RELION was also the first approach that forced division of the dataset of individual images into two completely independent halves at the very start of the processing and kept them separate throughout processing. This procedure produced Fourier Shell Correlation (FSC) plots that were termed 'gold-standard' following a discussion at a meeting of the EM validation task force (EMVTF) in 2010 (Henderson *et al.* 2012). The importance of keeping the two halves of any dataset completely separate to avoid 'overfitting' of noise had been well established from the work of Grigorieff (Grigorieff, 2000; Stewart & Grigorieff, 2004), but was unpopular because it gave less optimistic (although realistic) resolution estimates. RELION uses the gold-standard FSC curves to estimate the signal level in the dataset of images, to filter the projections used for orientation determination, and to produce 3D maps with more reliable resolution estimates

7

(Scheres & Chen, 2012). The resolution-limited refinement of particle orientations is also an important principle that can be used to avoid 'overfitting' and has always been a recommended feature in Frealign (Grigorieff, 2007). Many other improvements in the different packages have been made that are too detailed to be described here. For example, EMAN uses a spectral-signal-to-noise-ratio weighted Fourier Ring Correlation (FRC) integral alongside other similarity metrics for particle registration.

Elmlund introduced SIMPLE (Elmlund & Elmlund, 2012) and PRIME (Elmlund et al. 2013) with the goal of transforming raw 2D single particle images into an initial model of a 3D structure with no information other than the pixel size and the expected particle size. Although this ignored the CTF completely, which limited the resolution of the resulting structures to around 20 Å, it worked very well on homogeneous datasets.

Three-dimensional classification was originally implemented within Xmipp (Sorzano et al. 2004) and improved by addition of a ML-scoring system (Scheres et al. 2005, 2007a, b). Applied to a pre-existing ribosome dataset, this resulted in identification of two key conformational states showing that the images consisted of a mixture of two principal ribosomal complexes. The major population had tRNA in each of the three A, P and E sites, and the minor population had bound elongation factor EF-G and a single tRNA. Later work with 3D classification in RELION on the same dataset of images, showed the additional presence of about 10% of particles that contained only the large subunit (Scheres, 2012). ML 3D classification has recently also been implemented in Frealign (Lyumkis et al. 2013) with accompanying improvements in structure quality.

4. Outstanding issues and barriers to progress

4.1 Detector development

Further improvements in detector performance require solving one or two remaining problems. First it is important that detectors should be developed so that their DQE is as close as possible to 100%. This will require universal adoption of electron counting since the distribution of energy deposition when individual electrons pass through any detector is stochastic (Fig. 4) and the so-called Landau distribution (Fig. 5) has a very wide spread. Electron counting can be done on any of the current CMOS detectors but is too slow for normal use unless the frame rate is high. A reasonably high frame rate is already available commercially with the Gatan K2/Summit detector (Li et al. 2013a). Any implementation of electron counting will benefit from minimising missed or overlapping events, which requires a high signal-to-noise ratio and a high frame rate. Improving the signal-to-noise ratio of the read-out helps to minimise missed events. A larger pixel size would allow the use of a thicker epilayer with a resulting increased signal, and a greater degree of backthinning reduces the incidence of electron tracks, where the incident electron is scattered through 90° and tracks through several pixels. Accurate sub-pixel localisation is incompatible with events that appear as tracks. It should be possible for DQE(0) to approach 100%, and there are reasonable prospects for an increase in DQE(Nyquist) to 80–90%. A very small number of electrons will always be backscattered elastically from the detector surface without depositing any energy. Others may pass through and deposit very little energy so they may remain undetected, unless the epilayer is thick enough to improve signal-to-noise ratio. Others will be scattered sideways (Fig. 6) to leave tracks of deposited energy that contain no high resolution information. Finally, unless the frame rate is very high there will always be the temptation to increase the beam intensity thus increasing the number of overlapping events and reducing the overall DQE.

4.2 Beam-induced specimen movement

Although many groups are now obtaining outstanding results with this new generation of CMOS detectors, the number of particles or asymmetric units being used to obtain maps with resolutions in the 3–4 Å region is still in the range of 30 000–500 000, often greater (Vinothkumar, 2015). Thus instead of requiring 10 000x more particles than theory suggests are necessary, which was the situation a few years ago, we now need only 100x more in the best cases. Why are such large numbers of particles still needed? All the groups who have studied the information content in the movie time sequence have noticed that the first few frames, with electron doses of 1–4 el Å^{-2}, contribute much less signal to the final structure than the frames that represent the exposure range from about 5–10 el Å^{-2} (Allegretti et al. 2014; Grant & Grigorieff, 2015; Liao et al. 2013; Scheres, 2014; Vinothkumar et al. 2014a). Figure 7 shows some examples of such plots. After an exposure of 10 el Å^{-2}, the signal generally decays as would be expected from the effects of radiation damage, which degrades the structure and replaces it with carbonaceous remains, from which hydrogen and other gases have been released by bond fission.

Probably the most important outstanding problem in cryoEM is to understand and cure this information loss, which is generally thought to be due to beam-induced specimen movement and charging. Our current understanding of some of the key aspects of single particle cryoEM is summarised first.

8
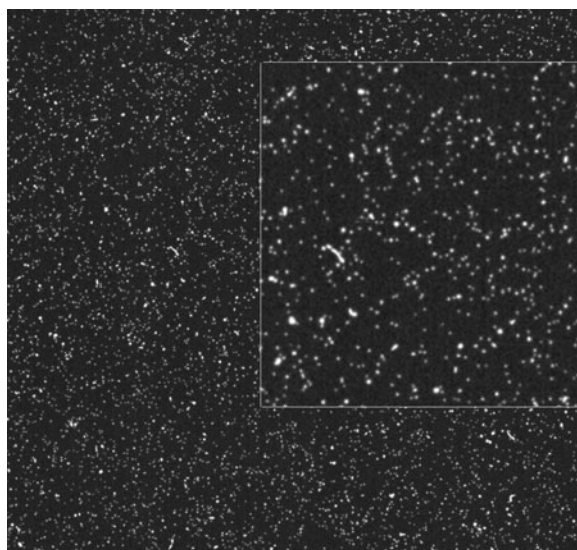
Fig. 4. Single frame image recorded using 300 keV electrons, showing single electron events on an FEI Falcon III detector, with excellent signal-to-noise ratio. Falcon III is a highly backthinned sensor with very low noise level. The single frame shows about 100 000 electron events (i.e. one electron per 150 pixels). This figure is similar to that for Falcon III in Kuijper *et al.* (2015).
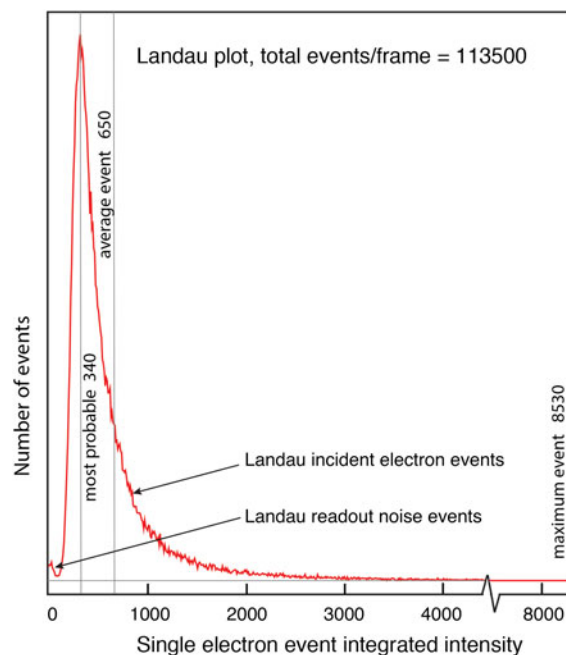
Fig. 5. Landau distribution for the single electron events from the image shown in Fig. 4. Single electron events are identified by an initial threshold criterion and then all pixels contributing to each event are added together to determine the total signal from each electron. The Landau plot is the histogram of the single-electron event distribution.

Following the preparation of samples for cryoEM using the method of Dubochet *et al.* (1982,1984), we typically apply a small drop (3 μl) of a solution of the biological structure of interest to a holey carbon film on a metal EM grid. This is then blotted for a few seconds (using filter paper) and rapidly frozen by plunging the grid into liquid ethane cooled by liquid nitrogen to a temperature just above the freezing point of liquid ethane (−183 °C). The macromolecular structures of interest are thus suspended in this thin film and can be imaged after transfer at liquid nitrogen temperature into an electron cryomicroscope. There are several steps during the freezing process. During the initial stages of the plunge-freezing, the thin film, which is mostly water, is supercooled by the surrounding ethane sufficiently fast that ice crystals do not have time to nucleate and grow. Instead, the temperature of the thin film rapidly falls to −180 °C, resulting in low-density amorphous ice. Only in

9
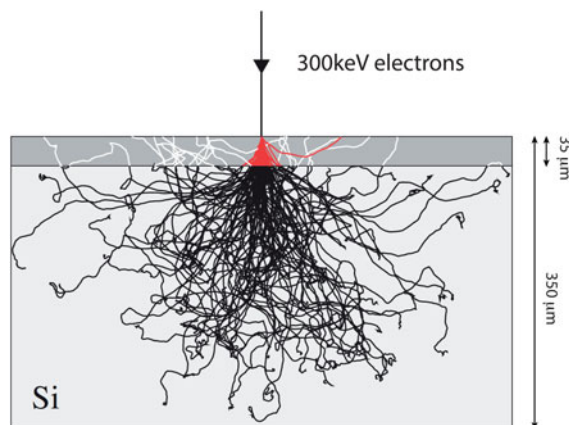
Fig. 6. Schematic of 300 keV electron trajectories, reproduced from McMullan *et al.* (2009c), showing a Monte Carlo simulation of 300 keV electron tracks in silicon. After backthinning to 35 μm, only those parts of the electron tracks highlighted in red would contribute to the recorded signal. Before backthinning, the additional white tracks would contribute a low-resolution component to the signal together with contributions to the noise at all spatial frequencies. The overall thickness of the silicon in the figure is 350 μm with the 35 μm layer that remains after backthinning shown in grey.
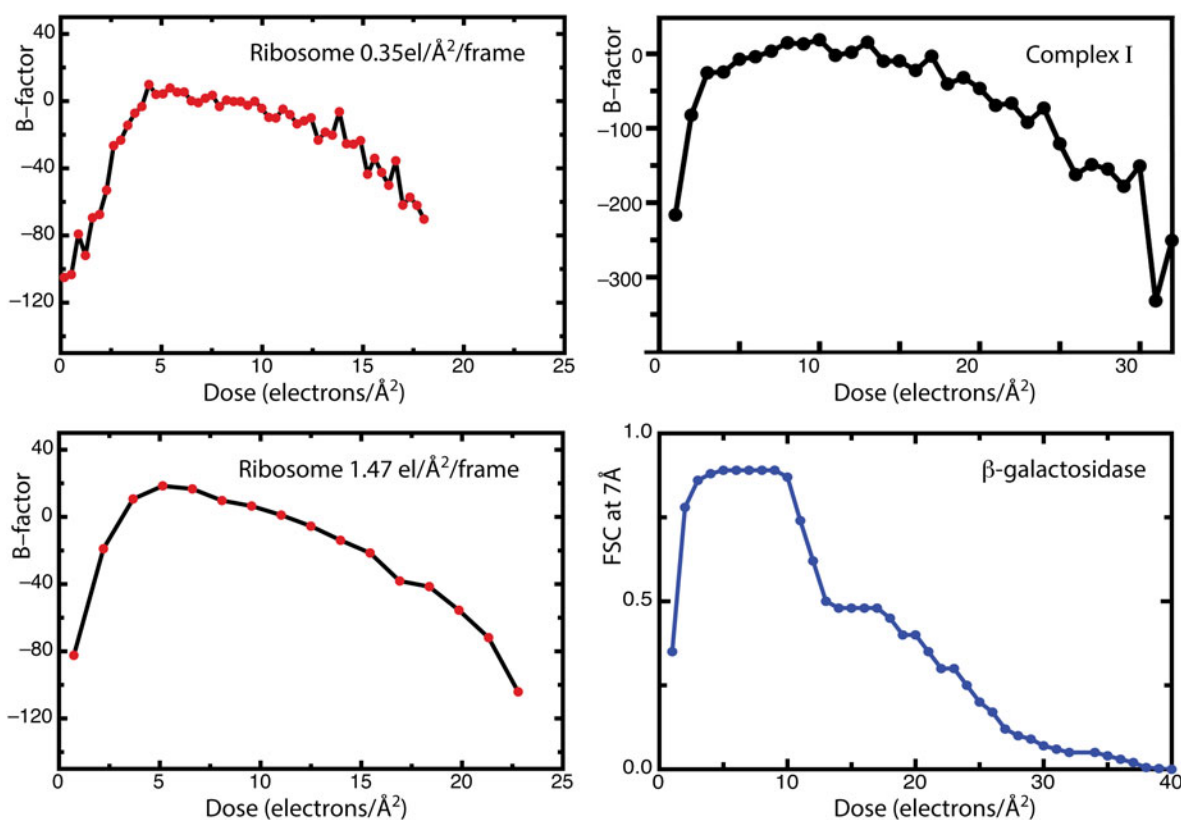
Fig. 7. Plot of the B-factors or signal at 7 Å resolution in typical movie sequences, reproduced from Henderson (2015) with permission.

regions near the metal grid bars of the EM grid does the temperature fall more slowly due to the thermal inertia of the grid bar, so there is a 3–5 μm wide region near each grid bar where the ice is frequently crystalline. The cooling process produces different volume changes in all three elements of the 'grid' structure, namely the metal framework, the support film and the ice.

First the width and spacing of the grid bars, which are normally made from copper or sometimes gold, shrinks by 0.2% as the temperature drops from 4 °C to −180 °C. Second, the carbon film shrinks by much less, since its coefficient of linear

10

expansion is ~10x less than copper. Thus the carbon film develops wrinkles as it cools, often termed cryo-crinkling (Booy & Pawley, 1993). Its behaviour as a relatively robust, rigid support at room temperature is transformed into that of a fairly floppy support film once cooled to liquid nitrogen temperature (Russo & Passmore, 2016). Russo & Passmore (2014a) have shown that supporting films of pure gold on gold grids do not have this problem so they move much less when irradiated in the electron microscope. Alternatively, tungsten or molybdenum grids can been used, because these metals have a lower linear expansion coefficient and less crinkling (Booy & Pawley, 1993; Glaeser, 1992; Vonck, 2000). In contrast to the carbon or gold film, the thin film of buffer with a density of ~1.0 g/cc expands as it is supercooled from 4 °C and continues to expand as it is transformed into amorphous ice, ending up with a density that has dropped to 0.93 g/cc, representing a 2.5% linear expansion (Dubochet et al. 1988). We believe that these differential changes in volume create stresses in the frozen film of amorphous ice, which are locked into the specimen at least until the electron beam is switched on.

Immediately after an exposure is initiated, the incident electron beam interacts with the specimen and a multitude of complicated processes are initiated. There is radiation damage to the water itself, and this causes movements of every water molecule by ~1 Å rms for every 1 e^- Å^{-2} of electron dose for 300 keV electrons (McMullan et al. 2015). Thus, after a total dose of 25 e^- Å^{-2} the water molecules have moved on average by ~5 Å. There is radiation damage to the protein that breaks bonds and creates free radicals. The bond breakage produces radiation products such as hydrogen, oxygen, methane and ethane, which are gases at liquid nitrogen temperature (Meents et al. 2010). Heavier fragments may be retained in a cavity in the specimen near to their original undamaged position. The bond breakage pushes the radiation products apart, for example, from 1.5 Å covalent separation to 3.5 Å van der Waals separation, and thus tends to expand the specimen, increasing the internal pressure. The evaporation of fragments however has the opposite effect, leaving gaps that would tend to collapse the structure. The relative balance between expansion and contraction is not known, but the greater amount of beam-induced specimen motion that is observed at liquid helium temperature, where most fragments – except for hydrogen gas – are solids, supports the idea that radiation damage to proteins and fragment production is a principal cause of beam-induced specimen motion. The increased pressure due to bond breakage also causes doming of the thin films of ice over holes in the supporting carbon film both at liquid nitrogen temperature (Campbell et al. 2012), and even worse at liquid helium temperature (Wright et al. 2006).

The motion of the water molecules during electron irradiation can be deduced from the observation of the strength of Thon rings in images of pure frozen water (McMullan et al. 2015). This beam-induced fluidity would be expected to allow the amorphous ice to move to relieve any stresses that were introduced during the original plunge-freezing of the specimen, as soon as the electron exposure is initiated. We now have three independent observations that in different ways demonstrate that the first 2–4 e^- Å^{-2} of the electron exposure are particularly important. First, we have the observation through the analysis of movie frames (Fig. 7) that the first few e^- Å^{-2} in any exposure contributes much less information to any structure determination than it should, presumably because of specimen motion or image blurring. Second, from the ice Thon ring measurements, we know that the water molecules themselves move to essentially new, uncorrelated positions at electron doses or 2–4 e^- Å^{-2}. Third, the publication by Wright et al. (2006) showed that the broad peak in the electron diffraction pattern of pure amorphous ice after irradiation at liquid helium temperature changes from ~3.7 to ~3.2 Å at electron doses of around 2 e^- Å^{-2}. They interpreted this as indicating a change in the density of the ice from low density to high density. Irrespective of whether their interpretation of their observations is correct, the key point is that exposures in the range of 1–2 e^- Å^{-2}, at both liquid nitrogen and liquid helium temperatures are sufficient to move water molecules to completely different positions. Several independent observations are thus consistent with a relaxation of the stresses in the amorphous ice structure during exposure to the first few electrons per Å^2, explaining why beam-induced specimen motion is worse at the beginning of a normal cryoEM exposure. Of course, the water molecules continue to move randomly during the later frames of a typical cryoEM image, but we hypothesise that the stresses have been relieved by this time and so any beam-induced motion is expected to be less systematic in subsequent frames, as observed. It is unclear whether this early period of stress removal involves only smooth motions or includes random jiggling.

How large is the loss of information from this early image blurring? This can be estimated from the known fading of electron diffraction patterns, such as observed for example with 2D crystals of bacteriorhodopsin. We have replotted the data from Stark et al. (1996) in Fig. 8, together with an extrapolation to 300 keV, using a scattering cross-section for 300 keV electrons that is 60% of that for 120 keV electrons, in proportion to the expected $1/(v^2/c^2)$ relationship, where v is electron velocity and c is speed of light. Stark et al. (1996) showed that the intensity of diffraction at liquid nitrogen temperature at 3 Å resolution for 120 keV electrons fades to 1% after 3 el Å^{-2} of exposure. By comparison, the diffraction at 7 Å resolution falls only to 50% of the initial intensity after an exposure of 3 el Å^{-2} at 120 keV (corresponding to 5 el Å^{-2} at 300 keV). Thus the 3 Å diffraction fades roughly 6x faster than the 7 Å diffraction, which translates into a B-factor of 90 Å^2 for typical exposures. This means that we may be losing only about half of the signal in images at 7–10 Å resolution at present through this beam-induced

11
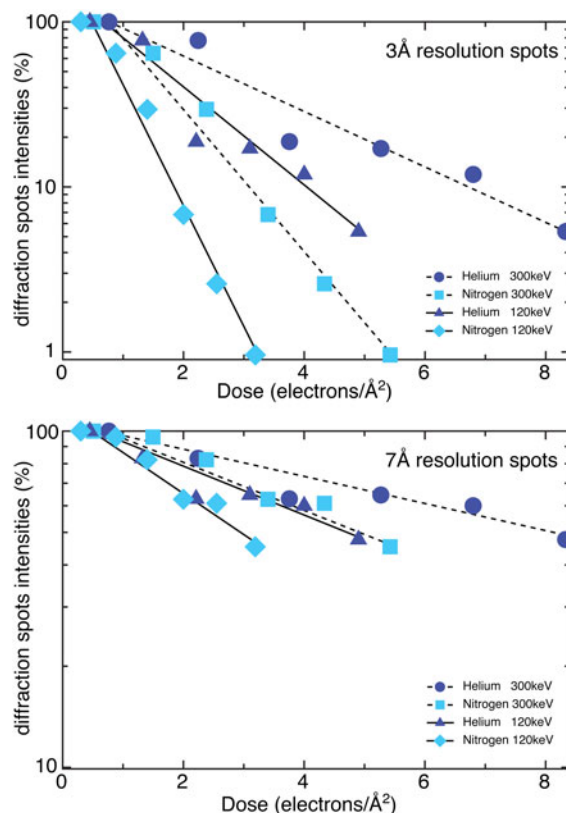
Fig. 8. Plots showing fading of electron diffraction spots at 7 Å and 3 Å resolution from 2D crystals of bacteriorhodopsin in purple membranes, replotted from Stark *et al.* (1996), comparing radiation damage at liquid helium and liquid N_2 temperatures. Note that the experimental measurements were made using 120 keV electrons. The solid line is the best fit to the experimental data. Since the fading should occur at 1.7x higher electron dose at 300 keV, the dashed line is an extrapolation. Image contrast is reduced for higher energy electrons but the longer exposures that are allowed compensate for the reduced contrast and make the signal-to-noise ratio very similar.

blurring effect, but as much as 98% of the signal at 3 Å resolution, even after alignment of individual frames. Coincidentally, this rough estimate agrees with the missing factor of 50–100 discussed at the beginning of this section.

In addition to these physical changes throughout the bulk specimen, the incident electron beam produces surface effects. There is mass loss from the two surfaces of the thin film that consists of hydrogen and oxygen gas that originates from the ice as well as volatised fragments of the protein. The rate of mass loss from the ice does not depend on thickness but is a purely surface effect (Heide, 1984), so radiation damage deeper inside the ice film involves recombination and annealing of hydrogen and oxygen-based radiation products.

Secondary electrons are also emitted from of the specimen, causing the illuminated area to become positively charged, especially on protruding regions or contamination where the ice surface is not completely flat. This positive charge on the specimen, if not neutralised by a compensating flow of electrons into the illuminated region, builds up during the exposure and causes either electrostatic lensing (Berriman & Rosenthal, 2012) that blurs the image (Fig. 9), or a tendency of the specimen physically to explode due to electrostatic repulsion forces.

There is a final concern. It is possible that microscopic charge fluctuations in ice-embedded specimens (because they are insulators) occur during normal cryoEM imaging conditions and that these fluctuations perturb the image throughout a normal exposure, affecting every frame of the dose-fractionated movie exposure series. This effect can be seen at very large defocus values as the well-known 'bee-swarm' effect (Brink *et al.* 1998; Curtis & Ferrier, 1969; Dove, 1964). We do not yet have enough quantitative analysis to know how well the experimental image frames compare with those from simulations limited only by radiation damage. Even if the current loss of information during the first few frames could be cured, it is possible that the entire exposure series is affected by microscopic electrostatic charging. If it is a serious factor, then one way round this would be to work at higher accelerating voltage, for example 1 or 3 MeV rather than 300 keV, though there are no modern cryEMs that have such a high operating voltage. The higher voltage would have the additional advantage of larger depth of field corresponding to a lower Ewald sphere curvature.

12
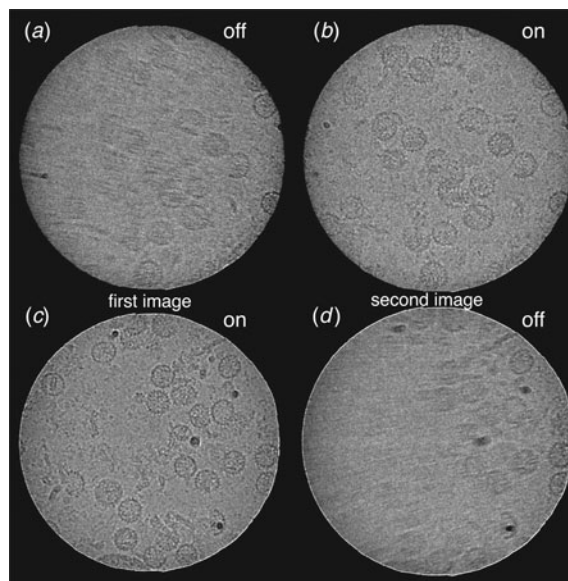
Fig. 9. Effect of paraxial illumination to neutralise positive charge build-up. This illustration of hepatitis B viral core uses the off-axis paraxial charge compensation procedure of Berriman & Rosenthal (2012) to reduce specimen charge build-up during exposure of an ice-embedded sample to an electron beam that has a smaller diameter than the hole in the holey carbon film. Panel (*a*) and (*b*) show images of the same region, in the absence (*a*) and presence (*b*) of the paraxial charge compensation. Panels (*c*) and (*d*) show a different area with the first image (*c*) now in the presence and the second image (*d*) in the absence of charge compensation. The blurring in (*a*) and (*d*) is caused by positive charge build-up. Six off-axis apertures in (*b*) and (*c*) illuminate regions of carbon film immediately adjacent to the hole, and these beams are blanked in (*a*) and (*d*), as described by Berriman & Rosenthal (2012). The diameter of the illuminating beam is ~4000 Å.

In summary, single particle cryoEM has already realised some of its potential and can currently be used to analyse structures quite well. However, with further efforts to address outstanding issues, the method should reach its full potential. The impact of these improvements will be to produce improved resolution, lead to a requirement for fewer particles, allow determination of orientations and structures of smaller particles, and allow the dissection of more multiple conformations from images of mixed populations.

4.3 Practical solutions to charging and movement

What can be done to minimise beam-induced specimen movement and charging? There is the possibility of using thicker support films (for example 500 Å thick amorphous carbon) that are still holey or gold films (Meyerson *et al.* 2014; Russo & Passmore, 2014a, 2016), which are more stable and electrically conductive than amorphous carbon. Glaeser *et al.* (2011) showed that images of paraffin on thick continuous carbon supports suffered from much less blurring due to beam-induced movement than on thin carbon supports (Glaeser *et al.* 2011). Gold grids are now available commercially from Quantifoil Micro Tools. There is also a possibility that smaller holes will provide a stronger supporting environment that will constrain any tendency to beam-induced motion. There are also efforts to explore the use of graphene support films (Pantelic *et al.* 2010; Russo & Passmore, 2014b; Sader *et al.* 2013), which could help to screen the incoming electron beam from any changes in internal specimen charge distribution, to supply new electrons to replace those ejected by beam damage and to prevent charge build-up.

Another possibility is to employ the equivalent of spotscan imaging (Bullough & Henderson, 1987; Downing, 1988, 1991), which was used successfully to decrease greatly the extent of beam-induced motion in images of 2D crystals, particularly when the specimen was highly tilted (Henderson *et al.* 1990). The idea behind spotscan is to illuminate only a small area of the specimen (the 'spot'), for example a circle of diameter ~1000 Å or smaller, at each moment followed by scanning or stepping the illuminating spot across the specimen to build up a complete image. Only the image of the illuminated region suffers from beam-induced blurring during the recording of the image of that spot and the surrounding unilluminated area acts as a robust anchor to minimise movement. The smaller illuminated diameter due to the small spot results in smaller movements.

For single particle specimens suspended in a thin film of ice this produces a problem that did not occur for 2D crystals supported on a carbon film. The illuminated area gets charged up and the resulting images are badly blurred due to electrostatic lensing. Berriman &

13
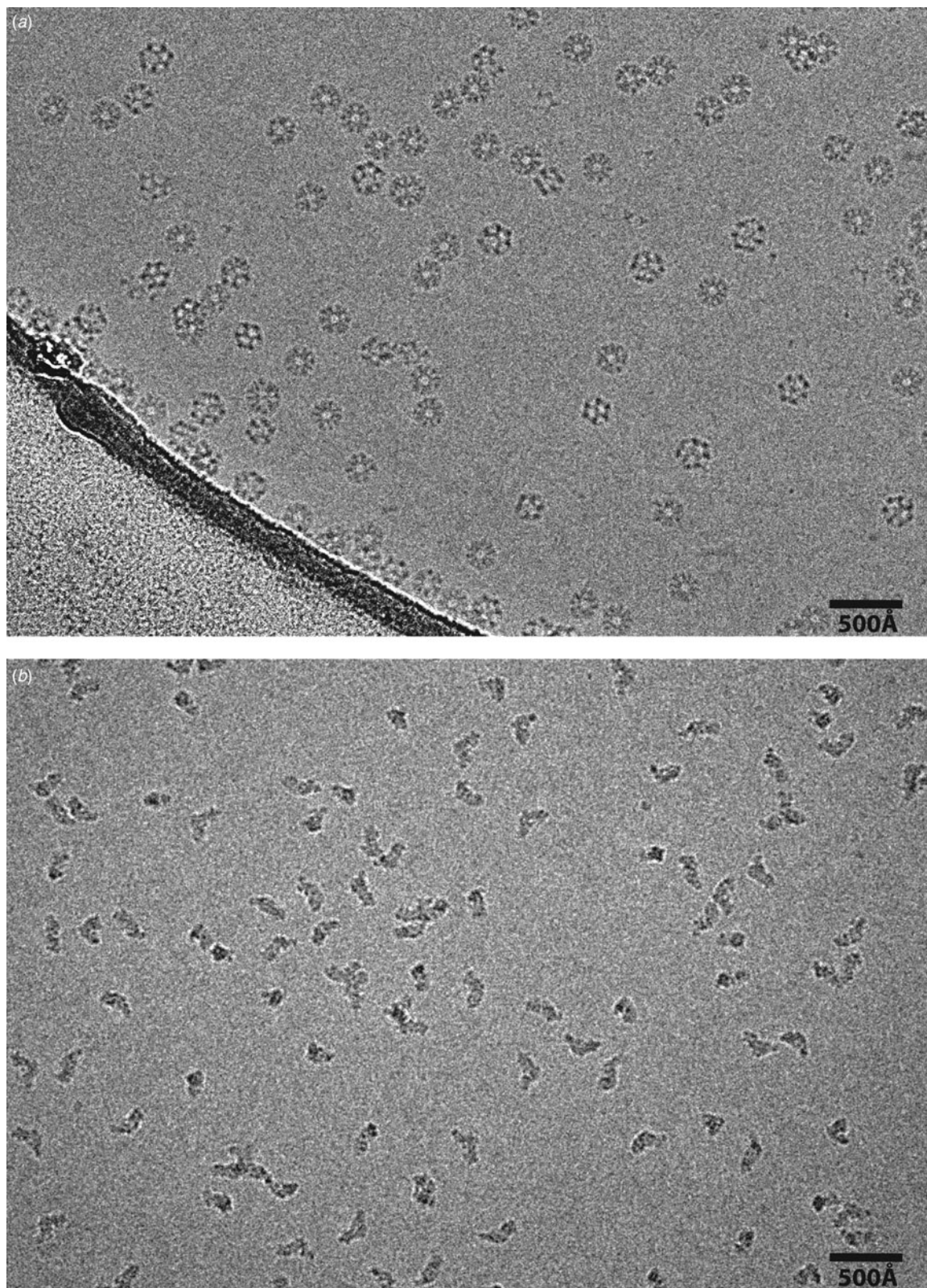
Fig. 10. Gallery of images of various specimens. Scale bars 500 Å. All the images shown in Figs 10 and 11 were taken at similar magnifications (1.75 Å/pixel) either on an FEI Polara or Krios at 3–4 μm defocus, 17 e Å^{-2} s^{-1} and 4s exposure. The images were taken on Falcon-II/III detectors, except for the β-galactosidase, which was taken on a K2 detector. (*a*) Pyruvate dehydrogenase E2CD, MW ~1.6MDa. Specimen prepared by Peter Rosenthal in 2001. 5-fold, 3-fold and 2-fold views are clearly visible. (*b*) Complex I, MW ~900 kDa (Vinothkumar *et al.* 2014b). (c) β-galactosidase, MW ~480 kDa (SigmaAldrich G3153; Chen *et al.* 2013). (d) Human erythrocyte catalase, MW ~240 kDa (SigmaAldrich C3566). The central empty region is where the ice is very thin. Surrounding this is a

14
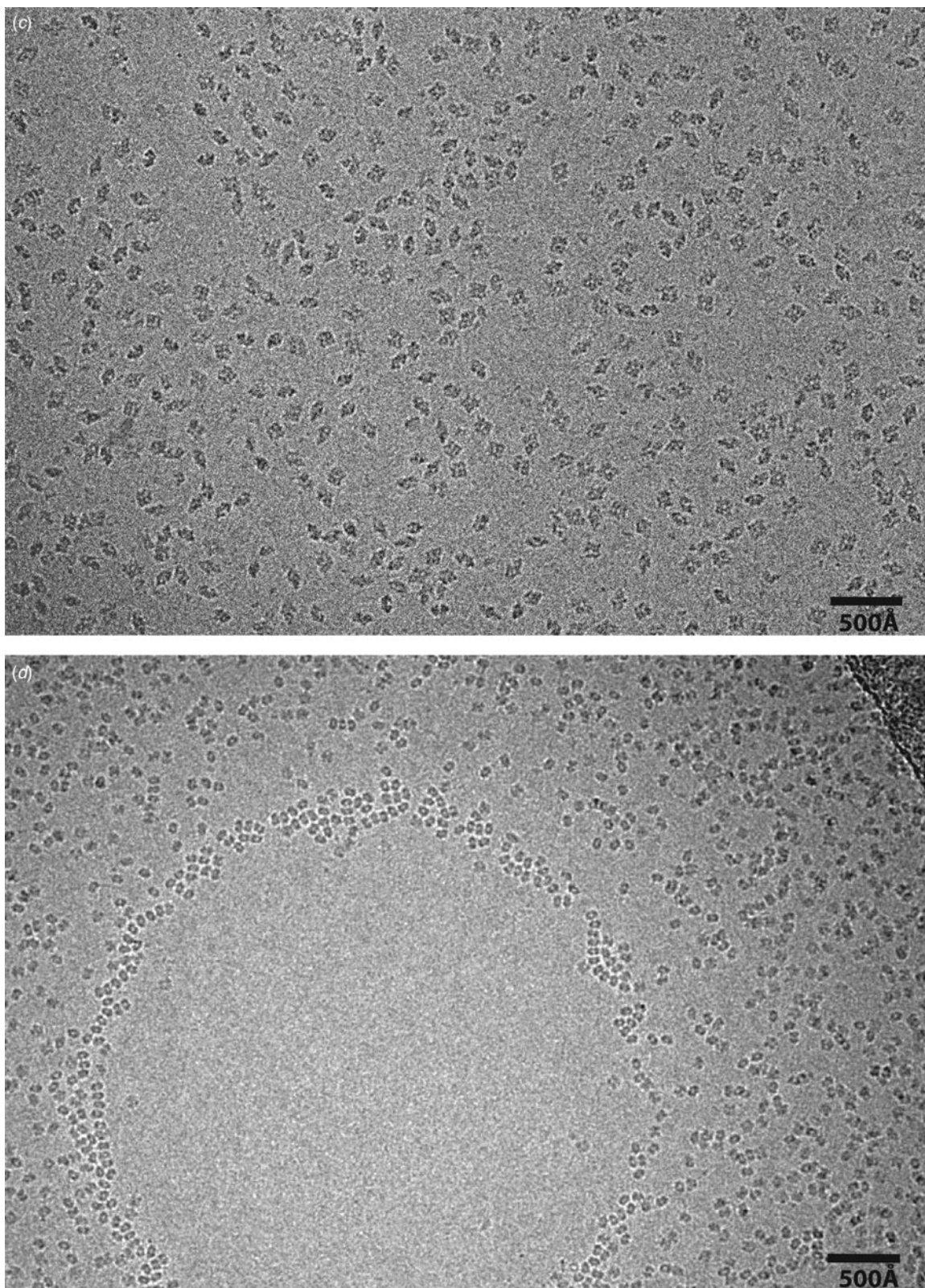
Fig. 10. (Continued).

circle of molecules where the catalase has been squeezed out and may be interacting with the air–water interfaces on both sides of the ice film. Further from the centre of the hole where the ice is thicker, the molecules are in random orientations and, once the ice gets much thicker at the edge of the hole, the molecules are even overlapping. (*e*) C-reactive protein, MW ~124 kDa pentamer (specimen courtesy

15

(e)

500Å

(f)

500Å
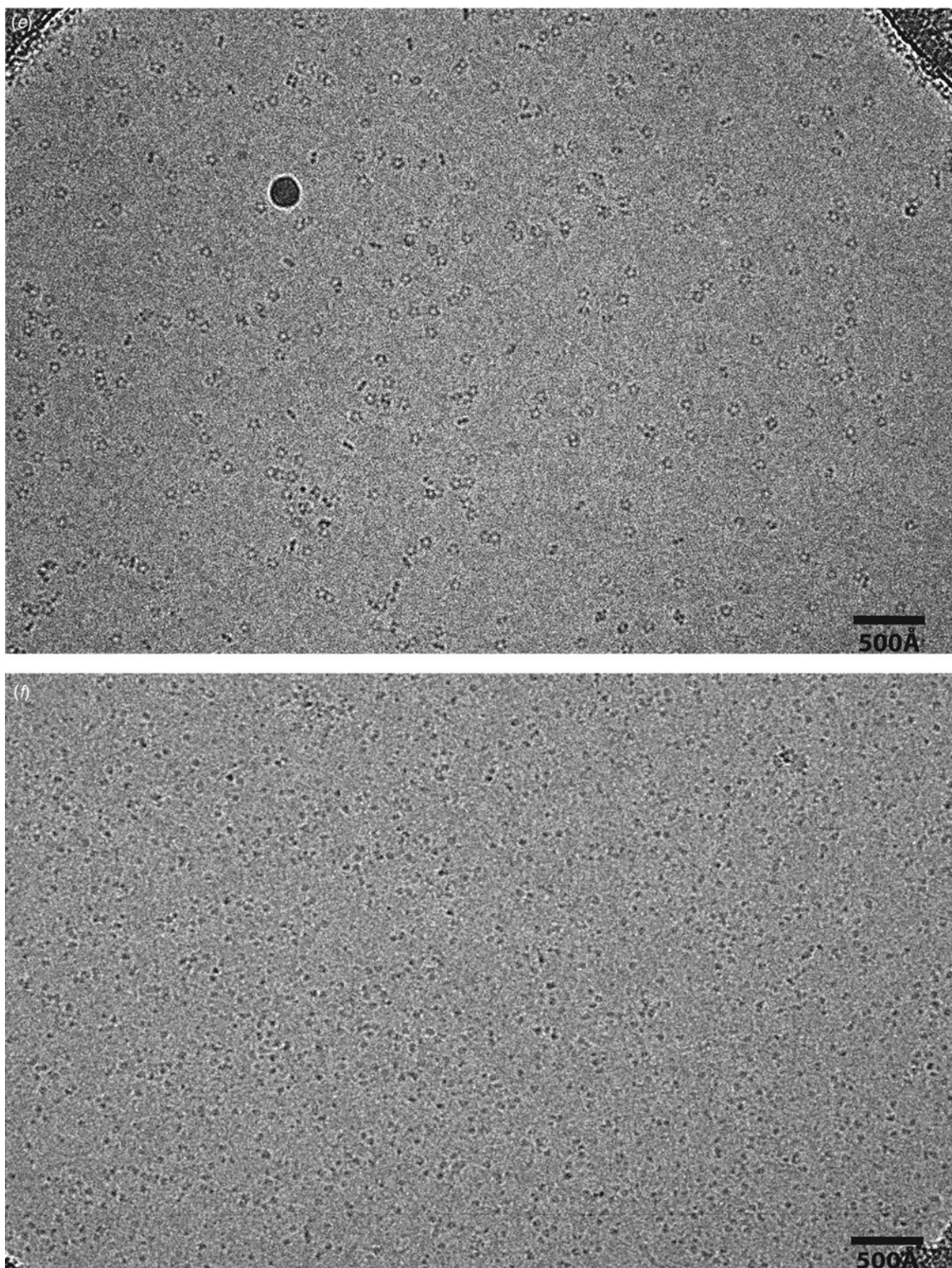
Fig. 10. (Continued).

of Glenys Tennent and Mark Pepys). Many 5-fold views are clearly visible with side views of the pentamers appearing as double dots or lines. Occasional decamers can be seen where the pentamers dimerise. (f) haemoglobin, MW 64 kDa (SigmaAldrich H7379). (g) ovalbumin, MW ~40 kDa (SigmaAldrich A5503). For these small proteins, the images appear as single dots. (h) lysozyme, MW ~14 kDa (SigmaAldrich L6876). Lysozyme molecules can be seen as individual very small dots, but still well above the noise level.

16

(g)

500Å

(h)

500Å
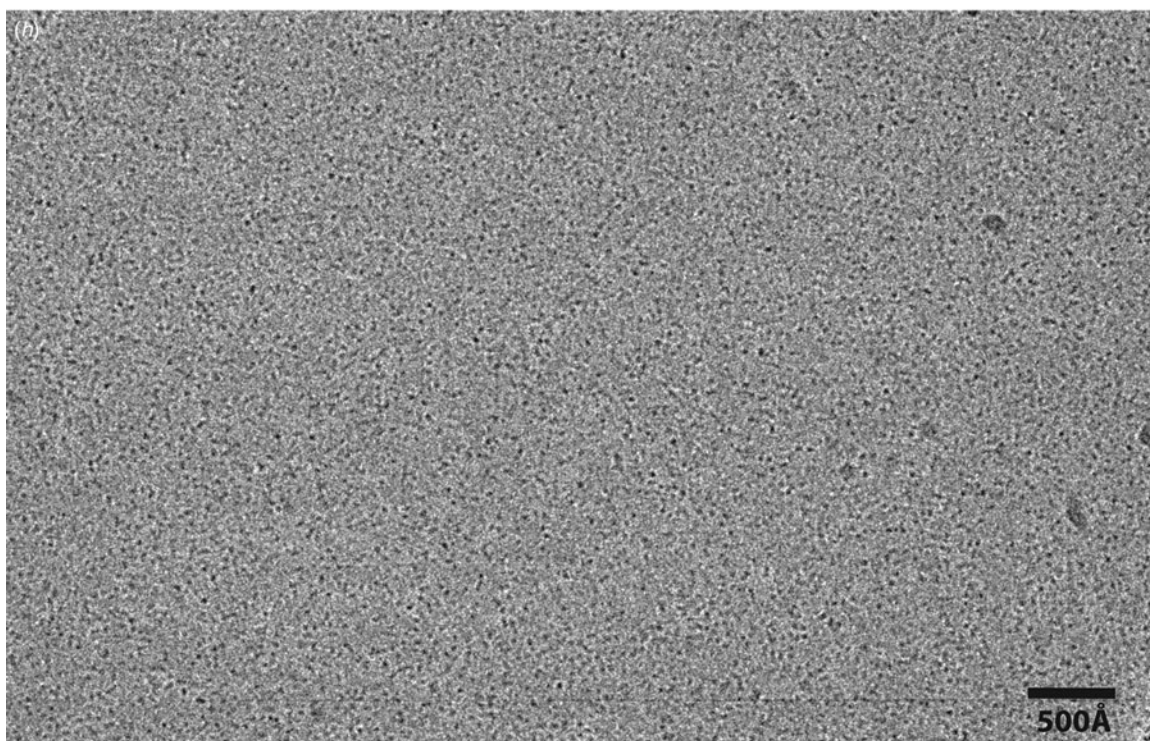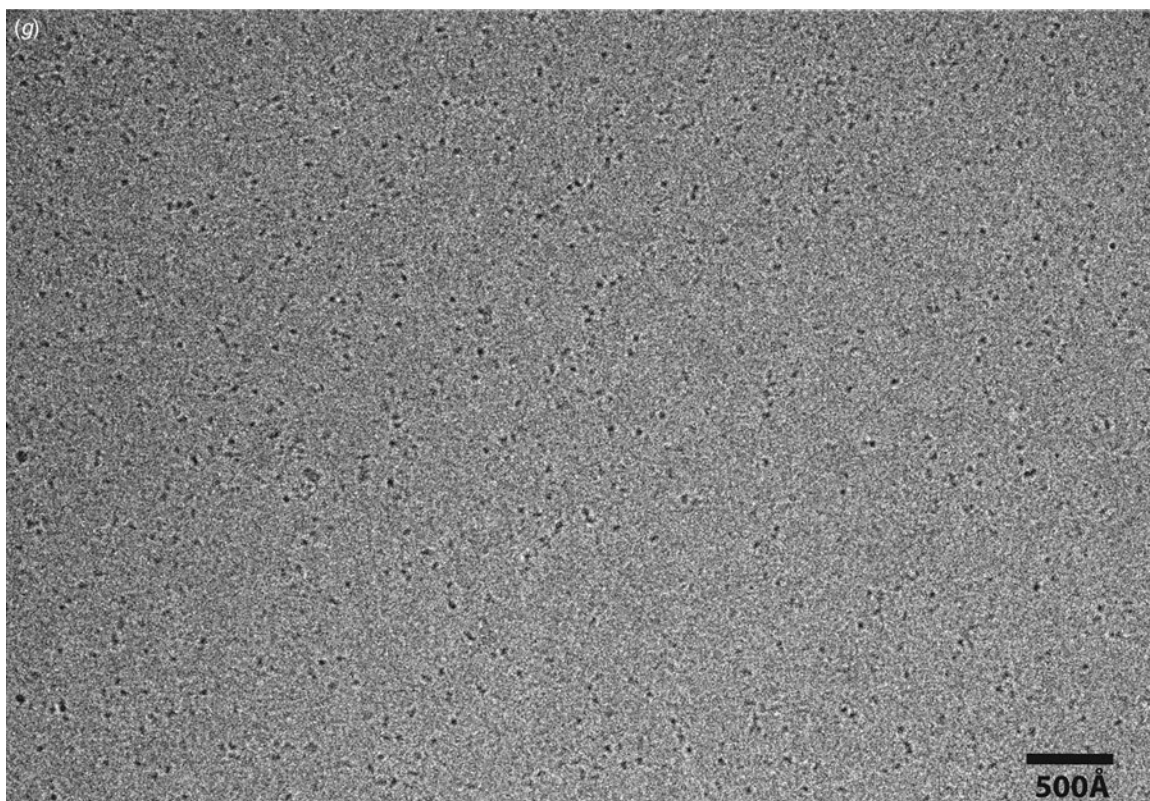
Fig. 10. (Continued).

Rosenthal (2012) developed a method to allow small spot illumination of an ice-embedded specimen that prevents charge build up. They used an off-axis multi-hole condenser aperture to provide paraxial illumination that effectively neutralised the charge on the ice by providing a source of secondary electrons to discharge it. They used up to 6 additional off-axis apertures to illuminate the

17

surrounding carbon film and showed that the degree of specimen charging was greatly reduced. The effect of using the Berriman & Rosenthal procedure is shown in Fig. 9 and may be useful for improving the quality of small spot imaging.

5. Need for affordable cryoEM

The technical details of cryoEM are important and can strongly affect the amount of effort required, the resolution obtained and the ability to resolve multiple states. At present, the performance advantage of 'high-end' cryoEM ('high' because of the large associated capital and running costs of a 300 keV facility) means that those groups and institutions that have access to the best equipment have an enormous advantage over those without such access. Since an installation with equipment that can deliver the best quality images can cost £5 M with annual running cost including management in the range of ~£250 000, this acts a barrier to providing access for research groups that are not located in a major centre. One solution to the problem would be to provide national (e.g. Saibil *et al.* (2015) for cryoEM in the UK) or international facilities best illustrated by the success and wide availability of third generation synchrotron sources for X-ray diffraction studies (e.g. ESRF, SPring-8).

The preparation of suitable specimens for cryoEM also requires a lot of preliminary evaluation. Alongside the need for excellent biochemistry, there are many pitfalls along the route to producing a perfect cryoEM grid with a good distribution of single particles that are not denatured at the air–water interface, aggregated, stuck to the support film or suffering from preferential orientations. To overcome this list of typical problems requires (preferably) daily access to a cryoEM facility that is good enough for characterisation of any specimen preparation problems, and for collection of small diagnostic datasets. High electron energy is not necessary in such a diagnostic tool since good images can be obtained at 100 keV. However, the coherence of the electron source makes an enormous difference to the detail visible in the highly defocussed images that are need to observe internal structure in smaller proteins. At present, it is not possible to interpret clearly images of protein assemblies of 150 kDa without the higher defocus that can be used with the much higher coherence of a field emission gun (FEG).

Thus alongside the availability of state-of-the-art 'high-end' electron cryomicroscopes, the structural biology field also desperately needs an inexpensive diagnostic cryoEM. Such an instrument is needed for preliminary evaluations, and should be able to achieve good enough resolution (e.g. 4 Å, which is enough to resolve the strands in β-sheets and some side-chain information) to evaluate the intrinsic quality of the specimens once a suitable particle distribution has been obtained. This local characterisation of specimens and grids could then feed into and make the best use of regional, national or international resources where higher resolution cryo-microscopes with greater automation could be available. It is certainly unrealistic to expect every laboratory to be able to afford a state-of-the-art facility, which at present needs to include a 300 keV Krios or similar high-end instrument, plus a direct electron detector and possibly also a zero-loss energy filter.

Given the cost of these higher voltage microscopes (due to the need for X-ray shielding and high voltage power supplies), it would be sensible to aim for a 100 or 120 keV instrument for the general market with a FEG electron source (500x brighter than a tungsten filament) and an efficient inexpensive detector at perhaps one tenth of the cost of the 'high-end' instruments.

6. Specimen preparation and gallery of cryoEM images

Single particle cryoEM has become very popular. While many of the recently determined structures have benefitted from years of careful biochemistry, there are also many other projects that are stuck at an earlier stage, often due to problems with biochemistry, or grid preparation alongside evaluation of cryoEM images. The main practical difficulty is to produce an even distribution of single particles without aggregation, suspended in a thin film of amorphous ice and with nearly random orientations so that all views are well represented. To get a good distribution of orientations, it often helps to add small amounts of detergents or explore different treatments of a thin carbon support film onto which the specimen is adsorbed, rather than using holey carbon or gold support films. Initially it is often not known what a particular specimen should look like and experience may be needed to know what to expect. As a result, it is good practice to pick the first set of single particles by hand (Henderson, 2013) rather than by using automated particle-picking procedures. A gallery of typical cryoEM images provides some useful common ground.

We show (Fig. 10) examples of cryoEM images of a series of monodisperse, well-behaved proteins such as a small icosahedral enzyme (1.6 MDa), mitochondrial Complex I (900 kDa), β-galactosidase (450 kDa), catalase (240 kDa), C-reactive protein (124 kDa), haemoglobin (64 kDa), ovalbumin (40 kDa) and lysozyme (14 kDa). All the images in Fig. 10 were taken under very similar conditions, as described in the legend. The smallest of these proteins appear simply as small dark dots without enough information to discern the orientation. As the structures get bigger it is possible to determine orientation, but the current minimum size for reliable orientation determination is in the range 100–200 kDa. Since many people are

18
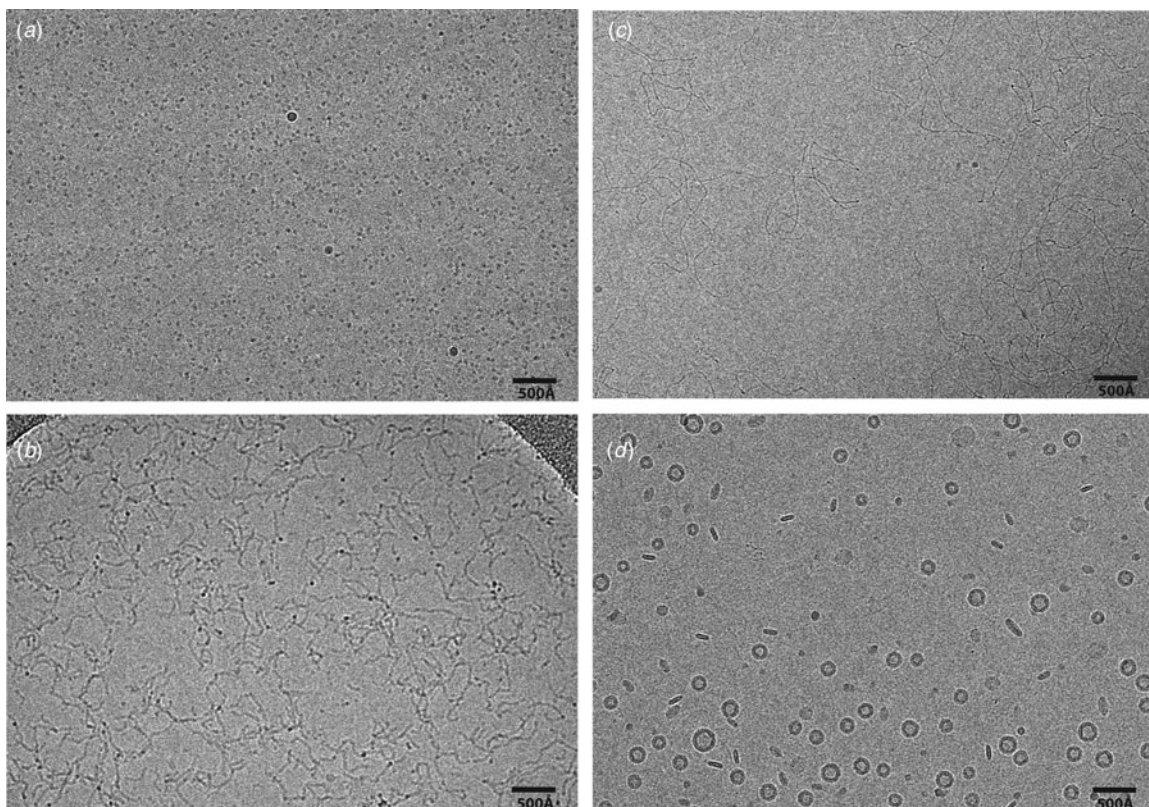
Fig. 11. Gallery of images of detergents, DNA, or lipid vesicles, which are often found in single particle cryoEM before optimisation of specimen preparation. Scale bar 500 Å. (*a*) DDM (Anatrace) 1%, showing lighter densities in the centre of each detergent micelle. (*b*) LMNG (Anatrace) 1%, showing aggregation into filamentous cylindrical micellar structures. (*c*) DNA (genomic DNA from *E.coli*), showing double-stranded filaments with an occasional hint of the 35 Å major groove periodicity. (*d*) Small spherical lipid vesicles with a small proportion of bilayer disks. POPC lipids (25 mg ml^{-1}) in chloroform (Avanti polar lipids) were dried under argon and the film resuspended in 1% decylmaltoside solution to give a final concentration of 5 mg ml^{-1}. For making liposomes, the detergent was dialysed out with buffer exchanged twice over 2 days. The liposome solution was passed through an extruder with a 0.1 μm filter and subsequently used for plunge-freezing.

trying to use cryoEM to analyse the structure of membrane proteins or membrane protein complexes, we also show some images (Fig. 11*a* and *b*) of pure detergent micelles or micellar/tubular structures that are often found after very dilute protein samples containing detergent are concentrated during the final step of purification. These detergent structures may appear alongside images of the desired membrane protein:detergent complex and for smaller membrane proteins are virtually indistinguishable. For completeness, some images of DNA (Fig. 11*c*) and lipid vesicles (Fig. 11*d*) are also shown. Even with preparations believed to represent pure monodisperse membrane proteins where we hope to see a nice distribution of single particles, cryoEM images often reveal the presence of everything except the one thing that is being looked for. Such images sometimes show features recognisable as detergent micelles, liposomes, aggregated protein and/or DNA impurities, sometimes all in the same image. We hope this gallery will help with the interpretation of sample preparation problems so that appropriate steps can be taken to overcome them. It is also useful to know how many particles should be expected in a typical image, assuming the single particles behave as if in free solution. Figure 12 shows a table of the expected particle density for different sized macromolecular complexes at different concentrations on holey grids. The legend gives some possible explanations for why more or less particles than this are often found.

There are a few other issues that occur frequently enough to be worth noting here. Purified proteins are often relatively unstable but the stability can be improved in the presence of 10 or 20% glycerol. Since high glycerol concentrations in the electron beam makes the frozen specimen more susceptible to radiation damage, it is usually wise to change the buffer to a glycerol-free medium immediately before preparing grids using a small spin-column. In a similar vein, salt concentrations above about 0.5 M can increase the background contrast in the image, especially if there is some evaporation during the blotting procedure, so it is best to aim for the lowest salt concentration that is compatible with the stability of the protein or macromolecular complex being investigated. Finally, one unsolved problem concerns the deleterious effect of the air–water interface. During the blotting procedure, the specimen is exposed to the air-water surface on one or both sides of the thin film of buffer for a period of several seconds, depending on whether the drop of specimen solution is adsorbed to a thin continuous carbon film or applied to a holey carbon

19

Number of particles in projection/μm² in 800 Å thick ice film (separation)

M.W.	Concentration				
	10mg/ml	2mg/ml	0.5mg/ml	0.1mg/ml	20μg/ml
10 kD	48000 (45Å)	10000 (100Å)	2500 (200Å)	500 (450 Å)	100 (1000 Å)
50 kD	10000 (100Å)	2000 (220Å)	500 (400Å)	100 (1000Å)	20 (0.2μm)
250kD	2000 (220Å)	400 (500 Å)	100 (1000 Å)	20 (0.2μm)	4 (0.5μm)
1 MD	500 (400Å)	100 (1000Å)	25 (0.2μm)	5 (0.4μm)	1 (1μm)
5 MD	100 (1000Å)	20 (0.2μm)	5 (0.4μm)	1 (1μm)	0.2 (2.2μm)
25 MD	20 (0.2μm)	4 (0.5μm)	1 (1μm)	0.2 (2.2μm)	0.04 (5μm)

Fig. 12. Expected particle distribution on holey grids. The table lists the expected number of single particles in cryoEM, answering the question 'Given the concentration of the molecule of interest in mg ml^{-1} and the molecular weight (MW), how many particles should you see in the image if the frozen specimen has the same concentration of molecules that you expect in free solution'. The number per μm² is given, as well as the expected particle separation for 800 Å thick ice. The boxes shown in red represent a distribution that is too dense, those in blue too sparse, and those in green about right. If images for the grid show either many more or many less particles than this, then something unexpected is going on. For example all the particles might be sticking to the carbon (if too few are seen in the holes) or the blotting operation might be concentrating the particles (if there are too many), but many different explanations are possible.

film. It is well known that proteins are adsorbed and frequently denatured at most surfaces (Ramsden, 1994), including the air-water surface, and the thickness of the adsorbed layer increases with time. Clearly, it would be advantageous to plunge-freeze the thin film as soon as possible after its formation to minimise the number of times the suspended particles interact with the surface.

7. Conclusion

Apart from the increased cost, further improvements in detector performance will produce virtually painless improvements in the attainable resolution, the amount of effort required or the ability to resolve multiple states using cryoEM. The biggest reward in terms of improved signal in high-resolution images or movies will come if the problem of beam-induced movement and image blurring in the early part of the exposure, corresponding to the first few frames of a movie could be cured. This may require some new approach to specimen preparation such as the use of a thicker support with smaller holes into which the ice-embedded molecules are trapped and frozen. Affordable entry-level instruments and more experience in specimen preparation will also be very useful. Progress may even come from new and unexpected approaches. Whatever happens, it is clear that cryoEM has a promising future.

Acknowledgements

References

ADRIAN, M., DUBOCHET, J., LEPAULT, J. & MCDOWALL, A. W. (1984). Cryo-electron microscopy of viruses. *Nature* **308**, 32–36.

ALLEGRETTI, M., MILLS, D. J., MCMULLAN, G., KÜHLBRANDT, W. & VONCK, J. (2014). Atomic model of the F420-reducing [NiFe] hydrogenase by electron cryo-microscopy using a direct electron detector. *eLife* **3**, e01963.

AMUNTS, A., BROWN, A., TOOTS, J., SCHERES, S. H. W. & RAMAKRISHNAN, V. (2015). The structure of the human mitochondrial ribosome. *Science* **348**, 95–98.

ARMACHE, J. P., JARASCH, A., ANGER, A. M., VILLA, E., BECKER, T., BHUSHAN, S., JOSSINET, F., HABECK, M., DINDAR, G., FRANCKENBERG, S., MARQUEZ, V., MIELKE, T., THOMM, M., BERNINGHAUSEN, O., BEATRIX, B., SODING, J., WESTHOF, E., WILSON, D. N. & BECKMANN, R. (2010). Cryo-EM structure and rRNA model of a translating eukaryotic 80S ribosome at 5.5-angstrom resolution. *Proceedings of the National Academy of Sciences of the United States of America* **107**, 19748–19753.

BAI, X. C., FERNANDEZ, I. S., MCMULLAN, G. & SCHERES, S. H. W. (2013). Ribosome structures to near-atomic resolution from thirty thousand cryo-EM particles. *eLife* **2**, e00461.

BERRIMAN, J. A. & ROSENTHAL, P. B. (2012). Paraxial charge compensator for electron cryomicroscopy. *Ultramicroscopy* **116**, 106–114.

BOOY, F. P. & PAWLEY, J. B. (1993). Cryo-crinkling - what happens to carbon-films on copper Grids at low-temperature. *Ultramicroscopy* **48**, 273–280.

20

Bottcher, B., Wynne, S. A. & Crowther, R. A. (1997). Determination of the fold of the core protein of hepatitis B virus ky electron cryomicroscopy. *Nature* **386**, 88–91.

Brilot, A. F., Chen, J. Z., Cheng, A. C., Pan, J. H., Harrison, S. C., Potter, C. S., Carragher, B., Henderson, R. & Grigorieff, N. (2012). Beam-induced motion of vitrified specimen on holey carbon film. *Journal of Structural Biology* **177**, 630–637.

Brink, J., Sherman, M. B., Berriman, J. & Chiu, W. (1998). Evaluation of charging on macromolecules in electron cryomicroscopy. *Ultramicroscopy* **72**, 41–52.

Bullough, P. & Henderson, R. (1987). Use of spot-scan procedure for recording low-dose micrographs of Beam-sensitive specimens. *Ultramicroscopy* **21**, 223–229.

Campbell, M. G., Cheng, A. C., Brilot, A. F., Moeller, A., Lyumkis, D., Veesler, D., Pan, J. H., Harrison, S. C., Potter, C. S., Carragher, B. & Grigorieff, N. (2012). Movies of ice-embedded particles enhance resolution in electron cryo-microscopy. *Structure* **20**, 1823–1828.

Carragher, B., Kisseberth, N., Kriegman, D., Milligan, R. A., Potter, C. S., Pulokas, J. & Reilein, A. (2000). Leginon: an automated system for acquisition of images from vitreous ice specimens. *Journal of Structural Biology* **132**, 33–45.

Chen, S. X., McMullan, G., Faruqi, A. R., Murshudov, G. N., Short, J. M., Scheres, S. H. W. & Henderson, R. (2013). High-resolution noise substitution to measure overfitting and validate resolution in 3D structure determination by single particle electron cryomicroscopy. *Ultramicroscopy* **135**, 24–35.

Conway, J. F., Cheng, N., Zlotnick, A., Wingfield, P. T., Stahl, S. J. & Steven, A. C. (1997). Visualization of a 4-helix bundle in the hepatitis B virus capsid by cryo-electron microscopy. *Nature* **386**, 91–94.

Crowther, R. A., Derosier, D. J. & Klug, A. (1970). Reconstruction of 3 dimensional structure from projections and its application to electron microscopy. *Proceedings of the Royal Society of London Series a-Mathematical and Physical Sciences* **317**, 319–&.

Curtis, G. H. & Ferrier, R. P. (1969). The electric charging of electron-microscope specimens. *British Journal of Applied Physics (Journal of Physics D)* **2**, 1035–1040.

Danev, R., Buijsse, B., Khoshouei, M., Plitzko, J. M. & Baumeister, W. (2014). Volta potential phase plate for in-focus phase contrast transmission electron microscopy. *Proceedings of the National Academy of Sciences of the United States of America* **111**, 15635–15640.

De Ruijter, W. J. (1995). Imaging properties and applications of slow-scan charge-coupled-device cameras suitable for electron-microscopy. *Micron* **26**, 247–275.

Dejong, A. F. & Vandyck, D. (1993). Ultimate resolution and information in electron-microscopy. 2. The information limit of transmission electron-microscopes. *Ultramicroscopy* **49**, 66–80.

Dove, D. B. (1964). Image contrasts in thin carbon films observed by shadow electron microscopy. *Journal of Applied Physics* **35**, 1652–1653.

Downing, K. H. (1988). Observations of restricted beam-induced specimen motion with small-spot illumination. *Ultramicroscopy* **24**, 387–398.

Downing, K. H. (1991). Spot-scan imaging in transmission electron-microscopy. *Science* **251**, 53–59.

Downing, K. H. & Hendrickson, F. M. (1999). Performance of a 2k CCD camera designed for electron crystallography at 400 kV. *Ultramicroscopy* **75**, 215–233.

Dubochet, J., Adrian, M., Chang, J. J., Homo, J. C., Lepault, J., Mcdowall, A. W. & Schultz, P. (1988). Cryo-electron microscopy of vitrified specimens. *Quarterly Reviews of Biophysics* **21**, 129–228.

Dubochet, J., Adrian, M., Teixeira, J., Alba, C. M., Kadiyala, R. K., Macfarlane, D. R. & Angell, C. A. (1984). Glass-forming microemulsions- vitrification of simple liquids and electron-microscope probing of droplet-packing modes. *Journal of Physical Chemistry* **88**, 6727–6732.

Dubochet, J., Lepault, J., Freeman, R., Berriman, J. A. & Homo, J. C. (1982). Electron-microscopy of frozen water and aqueous-solutions. *Journal of Microscopy-Oxford* **128**, 219–237.

Egelman, E. H. (2007). Single-particle reconstruction from EM images of helical filaments. *Current Opinion in Structural Biology* **17**, 556–561.

Egelman, E. H. (2015). Three-dimensional reconstruction of helical polymers. *Archives of Biochemistry and Biophysics* **581**, 54–58.

Elmlund, D. & Elmlund, H. (2012). SIMPLE: Software for ab initio reconstruction of heterogeneous single-particles. *Journal of Structural Biology* **180**, 420–427.

Elmlund, H., Elmlund, D. & Bengio, S. (2013). PRIME: probabilistic Initial 3D model generation for single-particle cryo-electron microscopy. *Structure* **21**, 1299–1306.

Ermantraut, E., Wohlfart, K., Schulz, T. & Tichelaar, W. (1997). Quantifoil: a support foil with holes of pre-defined size, shape and arrangement. *European Journal of Cell Biology* **74**, 97–97.

Ermantraut, E., Wohlfart, K. & Tichelaar, W. (1998). Perforated support foils with pre-defined hole size, shape and arrangement. *Ultramicroscopy* **74**, 75–81.

Faruqi, A. R., Henderson, R., Pryddetch, M., Allport, P. & Evans, A. (2005). Direct single electron detection with a CMOS detector for electron microscopy. *Nuclear Instruments & Methods in Physics Research Section a-Accelerators Spectrometers Detectors and Associated Equipment* **546**, 170–175.

Faruqi, A. R., Henderson, R. & Subramaniam, S. (1999). Cooled CCD detector with tapered fibre optics for recording electron diffraction patterns. *Ultramicroscopy* **75**, 235–250.

Fischer, N., Konevega, A. L., Wintermeyer, W., Rodnina, M. V. & Stark, H. (2010). Ribosome dynamics and tRNA movement by time-resolved electron cryomicroscopy. *Nature* **466**, 329–333.

Frank, J., Penczek, P., Grassucci, R. & Srivastava, S. (1991). 3-dimensional reconstruction of the 70s *Escherichia-coli* ribosome in ice - the distribution of Ribosomal-Rna. *Journal of Cell Biology* **115**, 597–605.

21

FRANK, J., SHIMKIN, B. & DOWSE, H. (1981). Spider - a modular software system for electron image-processing. *Ultramicroscopy* **6**, 343–357.

FRANK, J. & VAN HEEL, M. (1982). Correspondence-analysis of aligned images of biological particles. *Journal of Molecular Biology* **161**, 134–137.

FUJIYOSHI, Y. (1998). The structural study of membrane proteins by electron crystallography. *Advances in Biophysics* **35**, 25–80.

GABASHVILI, I. S., AGRAWAL, R. K., SPAHN, C. M. T., GRASSUCCI, R. A., SVERGUN, D. I., FRANK, J. & PENCZEK, P. (2000). Solution structure of the *E. coli* 70S ribosome at 11.5 angstrom resolution. *Cell* **100**, 537–549.

GAN, L. & JENSEN, G. J. (2012). Electron tomography of cells. *Quarterly Reviews of Biophysics* **45**, 27–56.

GLAESER, R. M. (1971). Limitations to significant information in biological electron microscopy as a result of radiation damage. *Journal of Ultrastructure Research* **36**, 466–&.

GLAESER, R. M. (1992). Specimen flatness of thin crystalline arrays - influence of the substrate. *Ultramicroscopy* **46**, 33–43.

GLAESER, R. M. (1999). Review: electron crystallography: present excitement, a nod to the past, anticipating the future. *Journal of Structural Biology* **128**, 3–14.

GLAESER, R. M. (2013). Invited review article: methods for imaging weak-phase objects in electron microscopy. *Review of Scientific Instruments* **84**, 111101, 1–17.

GLAESER, R. M. (2016). How good can cryo-EM become? *Nature Methods* **13**, 28–32.

GLAESER, R. M., HAN, B.-G., CSENCSITS, R., KILLILEA, A., PULK, A. & CATE, J. H. D. (2016). Factors that influence the formation and stability of thin, cryo-EM specimens. *Biophysical Journal* **110**, 749–755.

GLAESER, R. M., MCMULLAN, G., FARUQI, A. R. & HENDERSON, R. (2011). Images of paraffin monolayer crystals with perfect contrast: minimization of beam-induced specimen motion. *Ultramicroscopy* **111**, 90–100.

GRANT, T. & GRIGORIEFF, N. (2015). Measuring the optimal exposure for single particle cryo-EM using a 2.6 °A reconstruction of rotavirus VP6. *eLife* **4**, e06980.

GRIGORIEFF, N. (1998). Three-dimensional structure of bovine NADH: ubiquinone oxidoreductase (Complex I) at 22 angstrom in ice. *Journal of Molecular Biology* **277**, 1033–1046.

GRIGORIEFF, N. (2000). Resolution measurement in structures derived from single particles. *Acta Crystallographica Section D-Biological Crystallography* **56**, 1270–1277.

GRIGORIEFF, N. (2007). FREALIGN: high-resolution refinement of single particle structures. *Journal of Structural Biology* **157**, 117–125.

GRIGORIEFF, N. & HARRISON, S. C. (2011). Near-atomic resolution reconstructions of icosahedral viruses from electron cryo-microscopy. *Current Opinion in Structural Biology* **21**, 265–273.

HAAS, D. J. & ROSSMANN, M. G. (1970). Crystallographic studies on lactate Dehydrogenase at −75 °C. *Acta Crystallographica Section B* **B26**, 998–1004.

HEIDE, H. G. (1984). Observations on ice layers. *Ultramicroscopy* **14**, 271–278.

HENDERSON, R. (1990). Cryoprotection of protein crystals against radiation-damage in electron and x-ray-diffraction. *Proceedings of the Royal Society B-Biological Sciences* **241**, 6–8.

HENDERSON, R. (1995). The potential and limitations of neutrons, electrons and x-rays for atomic-resolution microscopy of unstained biological molecules. *Quarterly Reviews of Biophysics* **28**, 171–193.

HENDERSON, R. (2013). Avoiding the pitfalls of single particle cryo-electron microscopy: Einstein from noise. *Proceedings of the National Academy of Sciences of the United States of America* **110**, 18037–18041.

HENDERSON, R. (2015). Overview and future of single particle electron cryomicroscopy. *Archives of Biochemistry and Biophysics* **581**, 19–24.

HENDERSON, R., BALDWIN, J. M., CESKA, T. A., ZEMLIN, F., BECKMANN, E. & DOWNING, K. H. (1990). Model for the structure of bacteriorhodopsin based on high-resolution electron cryomicroscopy. *Journal of Molecular Biology* **213**, 899–929.

HENDERSON, R. & GLAESER, R. M. (1985). Quantitative-analysis of image-contrast in electron-micrographs of beam-sensitive crystals. *Ultramicroscopy* **16**, 139–150.

HENDERSON, R., SALI, A., BAKER, M. L., CARRAGHER, B., DEVKOTA, B., DOWNING, K. H., EGELMAN, E. H., FENG, Z. K., FRANK, J., GRIGORIEFF, N., JIANG, W., LUDTKE, S. J., MEDALIA, O., PENCZEK, P. A., ROSENTHAL, P. B., ROSSMANN, M. G., SCHMID, M. F., SCHRODER, G. F., STEVEN, A. C., STOKES, D. L., WESTBROOK, J. D., WRIGGERS, W., YANG, H. W., YOUNG, J., BERMAN, H. M., CHIU, W., KLEYWEGT, G. J. & LAWSON, C. L. (2012). Outcome of the first electron microscopy validation task force meeting. *Structure* **20**, 205–214.

HENDERSON, R. & UNWIN, P. N. T. (1975). 3-dimensional model of purple membrane obtained by electron-microscopy. *Nature* **257**, 28–32.

HEYMANN, J. B. (2001). Bsoft: image and molecular processing in electron microscopy. *Journal of Structural Biology* **133**, 156–169.

HOHN, M., TANG, G., GOODYEAR, G., BALDWIN, P. R., HUANG, Z., PENCZEK, P. A., YANG, C., GLAESER, R. M., ADAMS, P. D. & LUDTKE, S. J. (2007). SPARX, a new environment for Cryo-EM image processing. *Journal of Structural Biology* **157**, 47–55.

HOPE, H., FROLOW, F., VONBOHLEN, K., MAKOWSKI, I., KRATKY, C., HALFON, Y., DANZ, H., WEBSTER, P., BARTELS, K. S., WITTMANN, H. G. & YONATH, A. (1989). Cryocrystallography of ribosomal particles. *Acta Crystallographica Section B-Structural Science* **45**, 190–199.

HOPE, H. & NICHOLS, B. G. (1981). High-speed single-crystal x-ray data-collection with conventional diffractometers. *Acta Crystallographica Section B-Structural Science* **37**, 158–161.

HOPPE, W., SCHRAMM, H. J., STURM, M., HUNSMANN, N. & GASSMANN, J. (1976). 3-Dimensional electron-microscopy of individual biological objects. 3. Experimental results on Yeast Fatty-Acid Synthetase. *Zeitschrift Fur Naturforschung Section a-a Journal of Physical Sciences* **31**, 1380–1390.

KABIUS, B., HARTEL, P., HAIDER, M., MULLER, H., UHLEMANN, S., LOEBAU, U., ZACH, J. & ROSE, H. (2009). First application of C-c-corrected imaging for high-resolution and energy-filtered TEM. *Journal of Electron Microscopy* **58**, 147–155.

Knauer, V., Hegerl, R. & Hoppe, W. (1983). 3-dimensional reconstruction and averaging of 30 S-ribosomal subunits of *Escherichia coli* from electron-micrographs. *Journal of Molecular Biology* **163**, 409–430.

Krivanek, O. L. & Mooney, P. E. (1993). Applications of slow-scan CCD cameras in transmission electron-microscopy. *Ultramicroscopy* **49**, 95–108.

Kuhlbrandt, W., Wang, D. N. & Fujiyoshi, Y. (1994). Atomic model of plant light-harvesting complex by electron crystallography. *Nature* **367**, 614–621.

Kuijper, M., Van Hoften, G., Janssen, B., Geurink, R., De Carlo, S., Vos, M., Van Duinen, G., Van Haeringen, B. & Storms, M. (2015). FEI's direct electron detector developments: embarking on a revolution in cryo-TEM. *Journal of Structural Biology* **192**, 179–187.

Lepault, J. & Leonard, K. (1985). 3-dimensional structure of unstained, frozen-hydrated extended tails of bacteriophage-T4. *Journal of Molecular Biology* **182**, 431–441.

Li, X. M., Mooney, P., Zheng, S., Booth, C. R., Braunfeld, M. B., Gubbens, S., Agard, D. A. & Cheng, Y. F. (2013a). Electron counting and beam-induced motion correction enable near-atomic-resolution single-particle cryo-EM. *Nature Methods* **10**, 584–590.

Li, X. M., Zheng, S. Q., Egami, K., Agard, D. A. & Cheng, Y. F. (2013b). Influence of electron dose rate on electron counting images recorded with the K2 camera. *Journal of Structural Biology* **184**, 251–260.

Liao, M. F., Cao, E. H., Julius, D. & Cheng, Y. F. (2013). Structure of the TRPV1 ion channel determined by electron cryo-microscopy. *Nature* **504**, 107–112.

Liu, H., Jin, L., Koh, S. B. S., Atanasov, I., Schein, S., Wu, L. & Zhou, Z. H. (2010). Atomic structure of human adenovirus by Cryo-EM reveals interactions among protein networks. *Science* **329**, 1038–1043.

Ludtke, S. J., Baldwin, P. R. & Chiu, W. (1999). EMAN: semiautomated software for high-resolution single-particle reconstructions. *Journal of Structural Biology* **128**, 82–97.

Lyumkis, D., Brilot, A. F., Theobald, D. L. & Grigorieff, N. (2013). Likelihood-based classification of cryo-EM images using FREALIGN. *Journal of Structural Biology* **183**, 377–388.

Marabini, R., Masegosa, I. M., Sanmartin, M. C., Marco, S., Fernandez, J. J., Delafraga, L. G., Vaquerizo, C. & Carazo, J. M. (1996). Xmipp: an image processing package for electron microscopy. *Journal of Structural Biology* **116**, 237–240.

McMullan, G., Chen, S., Henderson, R. & Faruqi, A. R. (2009a). Detective quantum efficiency of electron area detectors in electron microscopy. *Ultramicroscopy* **109**, 1126–1143.

McMullan, G., Clark, A. T., Turchetta, R. & Faruqi, A. R. (2009b). Enhanced imaging in low dose electron microscopy using electron counting. *Ultramicroscopy* **109**, 1411–1416.

McMullan, G., Faruqi, A. R., Clare, D. & Henderson, R. (2014). Comparison of optimal performance at 300 keV of three direct electron detectors for use in low dose electron microscopy. *Ultramicroscopy* **147**, 156–163.

McMullan, G., Faruqi, A. R., Henderson, R., Guerrini, N., Turchetta, R., Jacobs, A. & Van Hoften, G. (2009c). Experimental observation of the improvement in MTF from backthinning a CMOS direct electron detector. *Ultramicroscopy* **109**, 1144–1147.

McMullan, G., Vinothkumar, K. R. & Henderson, R. (2015). Thon rings from amorphous ice and implications of beam-induced Brownian motion in single particle electron cryo-microscopy. *Ultramicroscopy* **158**, 26–32.

Medalia, O., Weber, I., Frangakis, A. S., Nicastro, D., Gerisch, G. & Baumeister, W. (2002). Macromolecular architecture in eukaryotic cells visualized by cryoelectron tomography. *Science* **298**, 1209–1213.

Meents, A., Gutmann, S., Wagner, A. & Schulze-Briese, C. (2010). Origin and temperature dependence of radiation damage in biological samples at cryogenic temperatures. *Proceedings of the National Academy of Sciences of the United States of America* **107**, 1094–1099.

Meyer, R. R. & Kirkland, A. I. (2000). Characterisation of the signal and noise transfer of CCD cameras for electron detection. *Microscopy Research and Technique* **49**, 269–280.

Meyerson, J. R., Rao, P., Kumar, J., Chittori, S., Banerjee, S., Pierson, J., Mayer, M. L. & Subramaniam, S. (2014). Self-assembled monolayers improve protein distribution on holey carbon cryo-EM supports. *Scientific Reports* **4**, 7084.

Milazzo, A. C., Leblanc, P., Duttweiler, F., Jin, L., Bouwer, J. C., Peltier, S., Ellisman, M., Bieser, F., Matis, H. S., Wieman, H., Denes, P., Kleinfelder, S. & Xuong, N. H. (2005). Active pixel sensor array as a detector for electron microscopy. *Ultramicroscopy* **104**, 152–159.

Miyazawa, A., Fujiyoshi, Y. & Unwin, N. (2003). Structure and gating mechanism of the acetylcholine receptor pore. *Nature* **423**, 949–955.

Murata, K., Liu, X. A., Danev, R., Jakana, J., Schmid, M. F., King, J., Nagayama, K. & Chiu, W. (2010). Zernike phase contrast cryo-electron microscopy and tomography for structure determination at Nanometer and Subnanometer resolutions. *Structure* **18**, 903–912.

Nagayama, K. (2014). Biological applications of phase-contrast electron microscopy. *Methods in Molecular Biology* **1117**, 385–399.

Nogales, E., Wolf, S. G. & Downing, K. H. (1998). Structure of the alpha beta tubulin dimer by electron crystallography. *Nature* **391**, 199–203.

Pantelic, R. S., Meyer, J. C., Kaiser, U., Baumeister, W. & Plitzko, J. M. (2010). Graphene oxide: a substrate for optimizing preparations of frozen-hydrated samples. *Journal of Structural Biology* **170**, 152–156.

Petsko, G. A. (1975). Protein crystallography at sub-zero temperatures - Cryo-protective mother liquors for protein crystals. *Journal of Molecular Biology* **96**, 381–392.

Provencher, S. W. & Vogel, R. H. (1988). 3-dimensional reconstruction from electron-micrographs of disordered specimens. 1. Method. *Ultramicroscopy* **25**, 209–221.

Radermacher, M., Wagenknecht, T., Verschoor, A. & Frank, J. (1987). 3-dimensional reconstruction from a single-exposure, random conical tilt series applied to the 50s-Ribosomal subunit of *Escherichia-Coli*. *Journal of Microscopy-Oxford* **146**, 113–136.

Ramsden, J. J. (1994). Experimental methods for investigating protein adsorption-kinetics at surfaces. *Quarterly Reviews of Biophysics* **27**, 41–105.

Rosenthal, P. B. & Henderson, R. (2003). Optimal determination of particle orientation, absolute hand, and contrast loss in single-particle electron cryomicroscopy. *Journal of Molecular Biology* **333**, 721–745.

Rosenthal, P. B. & Rubinstein, J. L. (2015). Validating maps from single particle electron cryomicroscopy. *Current Opinion in Structural Biology* **34**, 135–144.

Rubinstein, J. L. & Brubaker, M. A. (2015). Alignment of cryo-EM movies of individual particles by optimization of image translations. *Journal of Structural Biology* **192**, 188–195.

Russo, C. J. & Passmore, L. A. (2014a). Ultrastable gold substrates for electron cryomicroscopy. *Science* **346**, 1377–1380.

Russo, C. J. & Passmore, L. A. (2014b). Controlling protein adsorption on graphene for cryo-EM using low-energy hydrogen plasmas. *Nature Methods* **11**, 649–652.

Russo, C. J. & Passmore, L. A. (2016). Ultrastable gold substrates: properties of a support for high-resolution electron cryomicroscopy of biological specimens. *Journal of Structural Biology* **193**, 33–44.

Sader, K., Stopps, M., Calder, L. J. & Rosenthal, P. B. (2013). Cryomicroscopy of radiation sensitive specimens on unmodified graphene sheets: reduction of electron-optical effects of charging. *Journal of Structural Biology* **183**, 531–536.

Saibil, H. R., Grunewald, K. & Stuart, D. I. (2015). A national facility for biological cryo-electron microscopy. *Acta Crystallographica Section D-Biological Crystallography* **71**, 127–135.

Scheres, S. H. W. (2012). RELION: implementation of a Bayesian approach to cryo-EM structure determination. *Journal of Structural Biology* **180**, 519–530.

Scheres, S. H. W. (2014). Beam-induced motion correction for sub-megadalton cryo-EM particles. *eLife* **3**, e03665.

Scheres, S. H. W. & Chen, S. X. (2012). Prevention of overfitting in cryo-EM structure determination. *Nature Methods* **9**, 853–854.

Scheres, S. H. W., Gao, H. X., Valle, M., Herman, G. T., Eggermont, P. P. B., Frank, J. & Carazo, J. M. (2007a). Disentangling conformational states of macromolecules in 3D-EM through likelihood optimization. *Nature Methods* **4**, 27–29.

Scheres, S. H. W., Nunez-Ramirez, R., Gomez-Llorente, Y., Martin, C. S., Eggermont, P. P. B. & Carazo, J. M. (2007b). Modeling experimental image formation for likelihood-based classification of electron microscopy. *Structure* **15**, 1167–1177.

Scheres, S. H. W., Valle, M., Nunez, R., Sorzano, C. O. S., Marabini, R., Herman, G. T. & Carazo, J. M. (2005). Maximum-likelihood multi-reference refinement for electron microscopy images. *Journal of Molecular Biology* **348**, 139–149.

Sigworth, F. J. (1998). A maximum-likelihood approach to single-particle image refinement. *Journal of Structural Biology* **122**, 328–339.

Sorzano, C. O. S., Marabini, R., Velazquez-Muriel, J., Bilbao-Castro, J. R., Scheres, S. H. W., Carazo, J. M. & Pascual-Montano, A. (2004). XMIPP: a new generation of an open-source image processing package for electron microscopy. *Journal of Structural Biology* **148**, 194–204.

Stagg, S. M., Lander, G. C., Pulokas, J., Fellmann, D., Cheng, A. C., Quispe, J. D., Mallick, S. P., Avila, R. M., Carragher, B. & Potter, C. S. (2006). Automated cryoEM data acquisition and analysis of 284742 particles of GroEL. *Journal of Structural Biology* **155**, 470–481.

Stark, H., Zemlin, F. & Boettcher, C. (1996). Electron radiation damage to protein crystals of bacteriorhodopsin at different temperatures. *Ultramicroscopy* **63**, 75–79.

Stewart, A. & Grigorieff, N. (2004). Noise bias in the refinement of structures derived from single particles. *Ultramicroscopy* **102**, 67–84.

Stewart, P. L., Burnett, R. M., Cyrklaff, M. & Fuller, S. D. (1991). Image-reconstruction reveals the complex molecular-organization of adenovirus. *Cell* **67**, 145–154.

Suloway, C., Pulokas, J., Fellmann, D., Cheng, A., Guerra, F., Quispe, J., Stagg, S., Potter, C. S. & Carragher, B. (2005). Automated molecular microscopy: the new Leginon system. *Journal of Structural Biology* **151**, 41–60.

Tang, G., Peng, L., Baldwin, P. R., Mann, D. S., Jiang, W., Rees, I. & Ludtke, S. J. (2007). EMAN2: an extensible image processing suite for electron microscopy. *Journal of Structural Biology* **157**, 38–46.

Taylor, K. A. & Glaeser, R. M. (1974). Electron-diffraction of frozen, hydrated protein crystals. *Science* **186**, 1036–1037.

Taylor, K. A. & Glaeser, R. M. (1976). Electron-microscopy of frozen hydrated biological specimens. *Journal of Ultrastructure Research* **55**, 448–456.

Thomanek, U. F., Parak, F., Mossbaue, R. L., Formanek, H., Schwager, P. & Hoppe, W. (1973). Freezing of Myoglobin crystals at high-pressure. *Acta Crystallographica Section A* **A 29**, 263–265.

Turchetta, R. (1993). Spatial-resolution of silicon microstrip detectors. *Nuclear Instruments & Methods in Physics Research Section a-Accelerators Spectrometers Detectors and Associated Equipment* **335**, 44–58.

Unwin, P. N. T. & Henderson, R. (1975). Molecular-structure determination by electron-microscopy of unstained crystalline specimens. *Journal of Molecular Biology* **94**, 425–440.

van Heel, M. (1987). Angular reconstitution - a posteriori assignment of projection directions for 3-D reconstruction. *Ultramicroscopy* **21**, 111–123.

van Heel, M. & Frank, J. (1981). Use of multivariate statistics in analyzing the images of biological macromolecules. *Ultramicroscopy* **6**, 187–194.

van Heel, M., Harauz, G., Orlova, E. V., Schmidt, R. & Schatz, M. (1996). A new generation of the IMAGIC image processing system. *Journal of Structural Biology* **116**, 17–24.

van Heel, M. & Keegstra, W. (1981). Imagic - a fast, flexible and friendly image-analysis software system. *Ultramicroscopy* **7**, 113–130.

van Heel, M. G. (1979). Imagic and its results. *Ultramicroscopy* **4**, 117–117.

Vigers, G. P. A., Crowther, R. A. & Pearse, B. M. F. (1986). 3-dimensional structure of clathrin cages in ice. *Embo Journal* **5**, 529–534.

Vinothkumar, K. R. (2015). Membrane protein structures without crystals, by single particle electron cryomicroscopy. *Current Opinion in Structural Biology* **33**, 103–114.

24

VINOTHKUMAR, K. R., MCMULLAN, G. & HENDERSON, R. (2014a). Molecular mechanism of antibody-mediated activation of beta-galactosidase. *Structure* **22**, 621–627.

VINOTHKUMAR, K. R., ZHU, J. P. & HIRST, J. (2014b). Architecture of mammalian respiratory complex I. *Nature* **515**, 80–84.

VOGEL, R. H., PROVENCHER, S. W., VONBONSDORFF, C. H., ADRIAN, M. & DUBOCHET, J. (1986). Envelope structure of Semliki forest virus reconstructed from Cryoelectron micrographs. *Nature* **320**, 533–535.

VONCK, J. (2000). Parameters affecting specimen flatness of two-dimensional crystals for electron crystallography. *Ultramicroscopy* **85**, 123–129.

WAGENKNECHT, T., GRASSUCCI, R. & FRANK, J. (1988). Electron-microscopy and computer image averaging of ice-embedded large ribosomal-subunits from *Escherichia-coli*. *Journal of Molecular Biology* **199**, 137–147.

WANG, Z., HRYC, C. F., BAMMES, B., AFONINE, P. V., JAKANA, J., CHEN, D. H., LIU, X. G., BAKER, M. L., KAO, C., LUDTKE, S. J., SCHMID, M. F., ADAMS, P. D. & CHIU, W. (2014). An atomic model of brome mosaic virus using direct electron detection and real-space optimization. *Nature Communications* **5**, 1–12.

WRIGHT, E. R., IANCU, C. V., TIVOL, W. F. & JENSEN, G. J. (2006). Observations on the behavior of vitreous ice at similar to 82 and similar to 12 K. *Journal of Structural Biology* **153**, 241–252.

YONEKURA, K., MAKI-YONEKURA, S. & NAMBA, K. (2003). Complete atomic model of the bacterial flagellar filament by electron cryomicroscopy. *Nature* **424**, 643–650.

ZENG, X., STAHLBERG, H. & GRIGORIEFF, N. (2007). A maximum likelihood approach to two-dimensional crystals. *Journal of Structural Biology* **160**, 362–374.

ZHANG, X., JIN, L., FANG, Q., HUI, W. H. & ZHOU, Z. H. (2010). 3.3 angstrom Cryo-EM structure of a nonenveloped virus reveals a priming mechanism for cell entry. *Cell* **141**, 472–482.

ZHANG, X., SETTEMBRE, E., XU, C., DORMITZER, P. R., BELLAMY, R., HARRISON, S. C. & GRIGORIEFF, N. (2008). Near-atomic resolution using electron cryomicroscopy and single-particle reconstruction. *Proceedings of the National Academy of Sciences of the United States of America* **105**, 1867–1872.